Hydroelastic slamming response in the evolution of a flip-through event during shallow-liquid sloshing

C. Lugni, A. Bardazzi, O. M. Faltinsen, and G. Graziani

Citation: Physics of Fluids (1994-present) **26**, 032108 (2014); doi: 10.1063/1.4868878
View online: http://dx.doi.org/10.1063/1.4868878
View Table of Contents: http://scitation.aip.org/content/aip/journal/pof2/26/3?ver=pdfcov
Published by the AIP Publishing

PHYSICS OF FLUIDS **26**, 032108 (2014)

Hydroelastic slamming response in the evolution of a flip-through event during shallow-liquid sloshing

C. Lugni,[1,2] A. Bardazzi,[1,3] O. M. Faltinsen,[2] and G. Graziani[3]
[1]*CNR-INSEAN: Italian Research Council - Institute for Marine Technology, Roma, Italy*
[2]*CeSOS/Centre for Autonomous Marine Operations and Systems (AMOS), Department of Marine Technology, NTNU, Trondheim, Norway*
[3]*DIMA - University of Rome "Sapienza," Roma, Italy*

(Received 7 June 2013; accepted 5 March 2014; published online 21 March 2014)

The evolution of a flip-through event [6] upon a vertical, deformable wall during shallow-water sloshing in a 2D tank is analyzed, with specific focus on the role of hydroelasticity. An aluminium plate, whose dimensions are Froude-scaled in order to reproduce the first wet natural frequency associated with the typical structural panel of a *Mark III* containment system, is used. (Mark III Containment System is a membrane-type tank used in the Liquefied Natural Gas (LNG) carrier to contain the LNG. A typical structural panel is composed by two metallic membranes and two independent thermal insulation layers. The first membrane contains the LNG, the second one ensures redundancy in case of leakage.) Such a system is clamped to a fully rigid vertical wall of the tank at the vertical ends while being kept free on its lateral sides. Hence, in a 2D flow approximation the system can be suitably modelled, as a double-clamped Euler beam, with the Euler beam theory. The hydroelastic effects are assessed by cross-analyzing the experimental data based both on the images recorded by a fast camera, and on the strain measurements along the deformable panel and on the pressure measurements on the rigid wall below the elastic plate. The same experiments are also carried out by substituting the deformable plate with a fully stiff panel. The pressure transducers are mounted at the same positions of the strain gauges used for the deformable plate. The comparison between the results of rigid and elastic case allows to better define the role of hydroelasticity. The analysis has identified three different regimes characterizing the hydroelastic evolution: a quasi-static deformation of the beam (regime I) precedes a strongly hydroelastic behavior (regime II), for which the added mass effects are relevant; finally, the free-vibration phase (regime III) occurs. A hybrid method, combining numerical modelling and experimental data from the tests with fully rigid plate is proposed to examine the hydroelastic effects. Within this approach, the measurements provide the experimental loads acting on the rigid plate, while the numerical solution enables a more detailed analysis, by giving additional information not available from the experimental tests. More in detail, an Euler beam equation is used to model numerically the plate with the added-mass contribution estimated in time. In this way the resulting hybrid method accounts for the variation of the added mass associated with the instantaneous wetted length of the beam, estimated from the experimental images. Moreover, the forcing hydrodynamic load is prescribed by using the experimental pressure distribution measured in the rigid case. The experimental data for the elastic beam are compared with the numerical results of the hybrid model and with those of the standard methods used at the design stage. The comparison against the experimental data shows an overall satisfactory prediction of the hybrid model. The maximum peak pressure predicted by the standard methods agrees with the result of the hybrid model only when the added mass effect is considered. However, the standard methods are not able to properly estimate the temporal evolution of the plate deformation.

 [http://dx.doi.org/10.1063/1.4868878]

I. INTRODUCTION

The wave impact phenomenon that may occur during the evolution of sloshing flows in a tank is an important issue for the safety of Liquefied Natural Gas (LNG) carriers. The violent free-surface motions in a sloshing tank generally occur when the wave-induced horizontal ship velocities, in roll and/or pitch, contain sufficient energy in the frequency band close to the lowest sloshing frequency of the tank. Then, slamming events may occur, which originate impulsively with accompanying large local loads that may compromise the integrity of the tank structure.

The technological solutions consolidated for oil tankers to damp the sloshing phenomena are unsuitable for the membrane-type prismatic LNG tanks: the need of maintaining low temperature inside the tank, in order to keep the gas at the liquid state, implies that the side walls, designed to provide a good thermal insulation and adequate mechanical properties, are not capable of supporting the damping devices (e.g., vertical baffles).

The full understanding of the physical phenomena and the accurate evaluation of the local loads in sloshing-induced slamming events is a challenge for research. Typically, LNG carriers can operate both in fully loaded and ballasted conditions: in both cases, sloshing phenomena matter. The filling height and the geometry of the tank influence the sloshing scenarios and the induced global and local loads on the walls of the tank. The sloshing motion of the liquid, in partially filled tanks with finite liquid depth, generates a standing wave that may cause the liquid impact against the roof of the tank; eventually with the formation of a large gas cavity entrapped.[2] Conversely, in ballasted conditions, when low filling depth of the tank, i.e., shallow liquid, conditions exist,[14,15] the occurrence of travelling bore waves propagating with high velocity back and forth into the tank may cause large slamming loads. Depending on the impact angle, several and complex scenarios can occur. For example, when the impact angle between liquid and wall is small, gas entrapment may happen leading to gas compression and its interaction with the free surface.[4,5] In contrast, for an incipient breaking wave approaching a vertical wall, flip-through events[6] or flat impacts may occur causing localized and large loads without any gas-entrapment.

In all these cases, when the typical temporal duration of the local load is comparable with a natural period of the structural mode contributing to large structural stresses, hydroelasticity matters,[7] and affects the integrity of the structure. As a consequence, the assessment of the structural strength of a LNG membrane tank exposed to the dynamic and impulsive sloshing loads requires the prediction of the hydroelastic response of the structure.

However, because of the difficulty in solving the hydroelastic problem and in scaling the structural properties of the complex and composite material constituting a LNG tank, both the fully coupled hydroelastic calculations and the hydroelastic experiments at model scale are still unsolved challenges.

Simplified methods are used during the design stage. The classification rules[10,11] suggest two calculation methods to assess the dynamic structural response to sloshing loads: (i) the Direct Dynamic Finite Element Analysis (FEA) uses the pressure loads measured during experiments carried out with a rigid model (properly scaled to prototype scale) as input of a dynamic FEA of the full scale structure; (ii) the Indirect Dynamic FEA uses the results from a static FEA multiplied by a correction factor obtained through the Dynamic Amplification Factor (DAF) curve. The DAF is the ratio between the maximum dynamic response and the maximum static response for a considered sloshing pressure rise time.

The present investigation pursues the experimental study of the kinematic and dynamical features of a flip-through event occurring on a vertical wall of a 2D sloshing tank in shallow water condition. The previous paper by Lugni *et al.*,[6] has emphasized how the maximum pressure at a fixed point of the impact area is a poor indicator for the maximum load, because of the extremely local behavior of the impact phenomena. In the present paper, the strain distribution along a vertical deformable

aluminium plate inserted in the rigid vertical wall of a sloshing tank has been measured in model tests to characterize the dynamical features of the local loads. Since the plate is clamped at the vertical ends, kept free at the lateral ones and the impacting flow is almost 2D, the plate is modeled as a beam. The sizes, the thickness and the structural properties of the deformable beam have been fixed in order to reproduce the lowest structural natural wet frequency of a prototype panel typically used in a Mark III containment system.[7] Geometric scaling is respected using

$$\lambda = \frac{L_P}{L_m}, \tag{1}$$

where L_P and L_m indicate the length of the tank in prototype (P) and model (m) scale, respectively. Since the considered response (pressure, strain) is a function of the frequency of oscillation of the structure σ, of the length L of the tank and of the gravity acceleration g, it follows from the Pi theorem that the non-dimensional response is a function of

$$\sigma\sqrt{\frac{L}{g}}. \tag{2}$$

Since gravity is involved, this is in general sense called Froude scaling. Although the complete scaling of the structural properties of a Mark III structural panel is far from the objective of the present work, a comprehensive hydroelastic model scale experiment is carried out, which reproduces the lowest natural wet frequency of a prototype panel. In Sec. II, a theoretical model is described to study the hydroelastic problem. Such a model is preliminarily used to define the scaling of the experimental model, whose set-up together with the dynamic response of the deformable plate is detailed in Sec. III. Section IV contributes to understand the role of hydroelasticity during the evolution of the flip-through phenomenon. Finally, in Sec. V the results of the proposed hydroelastic model are compared against the experiments and the results of two simplified models typically used at the design stage to assess the role of the hydroelastic effects.

II. THEORETICAL MODEL AND DYNAMIC SCALING

Because of the complex physical phenomena connected to the sloshing flow and the subsequent hydroelastic slamming, here we propose a simplified theoretical model to estimate when hydroelastic effects matter. A hybrid numerical-experimental method, which uses both the information coming from a simplified numerical hydroelastic model and the data from experiments carried out using a fully rigid tank, is proposed to solve it. The hybrid model recovers, at the global level, the contribution coming from the time variation of the added mass.

In general, hydroelasticity may involve a strong or a weak coupling between the loading and the response. In the former case, the response influences the wetted area and the free-surface deformation causing a time varying added mass effect and a nonlinear variation of the kinematic and dynamic field. When a weak coupling is assumed, a quasi-static approach can be used and the hydrodynamic load on a fully rigid structure forces the structural response.

A. Definition of the problem

A 2D square tank with length L and height H ($L = H$), partially filled with water up to a height h has been considered. An elastic beam of length l is placed at a vertical distance a from the tank bottom $y = 0$ (see Figure 1). It reproduces the structural behavior of a single Mark III structural panel fixed between the stiffeners of a LNG tank, hence double-clamped conditions hold. The geometric and structural properties of the beam are chosen to obey Froude scaling of the lowest natural frequency of the structural panel at full scale, that is, based on Eqs. (1) and (2):

$$\sigma_m = \sigma_P\sqrt{\lambda}. \tag{3}$$

Here σ_P and σ_m indicate the lowest natural frequency of the structural panel at prototype and model scale, respectively. The Euler beam theory describes the deformation $w(t, y)$ along the beam that is,

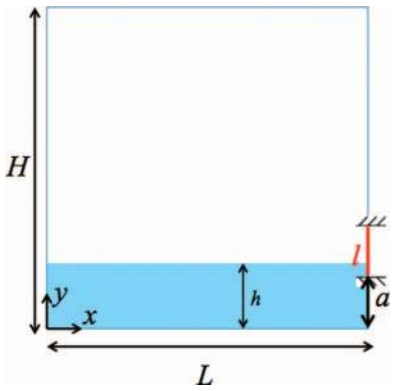

FIG. 1. Global sketch of the tank with the positioning of the elastic beam (red line).

for $a \le y \le a + l \quad x = L + w(t, y)$:

$$\begin{aligned} &M_B \frac{\partial^2 w}{\partial t^2} + \mu \frac{\partial w}{\partial t} + EI \frac{\partial^4 w}{\partial y^4} = p(t, y, w) \\ &w(t, a) = w(t, a + l) = 0 \\ &\frac{\partial w(t, y)}{\partial y}|_{y=a} = \frac{\partial w(t, y)}{\partial y}|_{y=a+l} = 0 \\ &\text{Initial Conditions on } w \text{ and } \frac{\partial w}{\partial t}. \end{aligned} \tag{4}$$

Here, M_B indicates the mass per unit length and breadth of the beam, μ the structural damping, I the inertial moment (i.e., area moment of inertia of the beam cross section/breadth of the beam), and E the Young's modulus of the material. On the right-hand side, $p(t, y, w)$ is the local hydrodynamic pressure load, which includes the mutual interactions between the structural deformations (and stresses) and the hydrodynamic flow. In order to know the pressure field $p(t, y, w)$, the solution of the hydrodynamic field for the sloshing problem is required. Because of the complex local phenomena involved in the sloshing flows (e.g., breaking waves, double phase flows, wave impacts) their numerical prediction requires, in general, the solution of the Navier-Stokes equation with nonlinear boundary conditions on the instantaneous air-water interface and on the wetted surfaces of the tank. This implies that along the beam, the following boundary condition holds

$$\frac{\partial w}{\partial t} = \boldsymbol{u} \cdot \boldsymbol{n}, \qquad a \le y \le a + l, \quad x = L + w(t, y), \tag{5}$$

where $\boldsymbol{u}$ is the local fluid velocity (a part in the liquid and a part in the air when air is entrapped, while it is assumed that the open air is at rest) and $\boldsymbol{n}$ is the local normal to the beam. The latter boundary condition, applied to the instantaneous deformable wetted beam, and the forcing pressure in the Euler equation, make the hydroelastic problem strongly coupled.

Colagrossi *et al.*[3] demonstrated that the simulation of the local flows characterizing the impact events in sloshing phenomena is complex, even when the tank is taken as fully rigid, which makes the use of the double-phase Navier-Stokes solvers unavoidable. On the other hand, the numerical simulation of a flip-through event can be done on the basis of potential flow assumptions, as assessed by Professor Peregrine.[12,13] In the present experimental investigation the analyzed flip-through event occurs during the third cycle of oscillation of the tank, after two previous oscillations during which some wave impact events occurred with air entrapped and vorticity was generated in the water as induced by the run down of the jet falling along the wall. These phenomena, in principle, preclude use of the potential flow theory to reproduce the hydrodynamic field that leads to the formation of the flip-through event of interest. However, since the main aim of the present paper is the physical discussion and assessment of the hydroelastic effects, we do not perform any numerical simulation

of the hydrodynamic field and, rather, in the following, we propose a simplified approach which takes into account the hydroelastic actions.

B. A simplified hydroelastic approach: The hybrid model

The proposed hybrid model is based on the assumption of a weak interaction between excitation and response, so that the forcing term in Eq. (4) can be decomposed as the followng linear superposition:

$$p(t, y, w) = p_r(t, y) + p_v(t, y, w).$$

The first contribution $p_r(t, y)$ is the pressure field induced by the flip-through event on the fully rigid wall, i.e., $\boldsymbol{u} = 0$ at $x = L$. It is a fully nonlinear load which depends on the nonlinear kinematics of the flip-through event and needs to be modeled as such. Because of the difficulty in reproducing it numerically, at least in the present case, we have chosen to model it using the experimental value of the pressure measured during the experiments on a fully rigid tank. During these experiments we reproduce exactly the same filling condition and tank motion used in the case of a deformable panel, hence the features of the wave interacting with the wall are the same.

The second contribution, $p_v(t, y, w)$, is the vibrational pressure, which solves the hydroelastic problem of the vibrating beam around a rest state. Using the potential flow assumption for an incompressible fluid with density ρ, the pressure forcing term $p_v = -\rho \frac{\partial \phi_v}{\partial t}$ is given by the linearized Bernoulli equation. The vibrational potential function is instantaneously determined as solution of the Boundary Value Problem (BVP):

$$\begin{aligned}
\nabla^2 \phi_v &= 0 && \text{in the water field} \\
\frac{\partial \phi_v}{\partial n} &= 0 && \text{on the rigid walls of the tank and on the bottom} \\
\frac{\partial \phi_v}{\partial n} &= \frac{\partial w}{\partial t} && a \le y < h(t) \quad x = L \\
\phi_v &= 0 && y = h(t) \quad 0 \le x \le L.
\end{aligned} \tag{6}$$

In this case we assume the vibrational pressure to be independent from the local shape of the free-surface and from the local kinematics of the flip through (which is already taken into account in the term p_r). However, p_v accounts for the instantaneous wetted length $h(t)$ of the vertical beam, influenced by the evolution of the flip-through. Because of the large value of the lowest wetted natural vibration frequency of the beam (with respect to the typical frequency range when gravity affects the free-surface behavior), a high-frequency approximation is assumed for the combined free-surface boundary condition. Although this is a strong approximation, we solve the problem through a simple approach and then verify the validity of the assumption through the comparison with the experiments. The above BVP for the Laplace equation is solved numerically as detailed in the following. Like p_r, also the wetted length $h(t)$ of the beam depends on the evolution of the flip-through, hence it cannot be predicted numerically and it has been measured from the experimental images.

The beam deflection $w(t, y)$ is expressed as the eigenfunction expansion of a finite number N of dry normal modes ψ_k, $k = 1...N$, satisfying the stationary homogeneous problem obtained from Eq. (4) with clamped conditions at the beam ends. Following Faltinsen and Timokha,[7] by defining $\dot{q}_k \phi_k$ the velocity potential associated with the vibrations of mode k, and assuming a proportional model for the structural damping, we get

$$[M + A(t)] \cdot \ddot{\boldsymbol{q}}(t) + [C] \cdot \dot{\boldsymbol{q}}(t) + [K] \cdot \boldsymbol{q}(t) = \int_l p_r(t, y) \boldsymbol{\psi}^{\boldsymbol{T}} dy \tag{7}$$

with

$$[M] = M_B \int_l \boldsymbol{\psi}\boldsymbol{\psi}^{\boldsymbol{T}} dy = M_B l[\mathcal{I}]$$

$$[A] = \rho \int_l \boldsymbol{\phi_v}\boldsymbol{\psi}^{\boldsymbol{T}} dy$$

$$[K] = EI(\frac{\boldsymbol{e}}{l})^4 \int_l \boldsymbol{\psi}\boldsymbol{\psi}^{\boldsymbol{T}} dy = EI(\frac{\boldsymbol{e}}{l})^4 l[\mathcal{I}]$$

which, respectively, are the mass, the hydrodynamic added mass and the stiffness matrices. The added mass matrix requires the solution of the BVP (6) for the vibrational potential function. By introducing the eigenfunction expansion for the beam deformation, the BVP (6) becomes

$$\begin{aligned} \nabla^2 \boldsymbol{\phi_v} &= 0 \\ \boldsymbol{\phi_v} &= 0 \qquad y = h(t) \\ \frac{\partial \boldsymbol{\phi_v}}{\partial n} &= \begin{cases} \boldsymbol{\psi}(t, y) & a \le y \le a + l, \quad x = L \\ 0 & \text{otherwise} \end{cases} \end{aligned} \tag{8}$$

and the potential vibrational vector $\boldsymbol{\phi_v}$ follows as solution of N Boundary Value Problems, each one corresponding to a prescribed vibrational mode of the beam.

Due to the orthogonality of the eigenfunction vector $\boldsymbol{\psi}$, the mass and stiffness matrices are diagonals ($[\mathcal{I}]$ is the identity matrix), while the added mass matrix is full. Structural damping $[C]$ is determined from the impulsive dry tests (hammer tests), as specified in Sec. III.

C. Numerical solution of the hybrid model.

The hydroelastic problem (7) is integrated in time using a fourth-order Runge-Kutta method to determine the mode amplitude vector $\boldsymbol{q(t)}$. At each time step, the forcing pressure $p_r(t, y)$ is prescribed by using the experimental pressure distribution measured through seven pressure transducers distributed along a rigid wall located like the beam in the fully rigid tank experiments (see Sec. III). In contrast, $\boldsymbol{\phi_v}$ comes from the numerical solution of the BVPs (8). For the latter, Faltinsen and Timokha[7] proposed an analytical solution assuming a Fourier expansion for $\boldsymbol{\psi}$ and $\boldsymbol{\phi_v}$. However, its validity is limited to the fully wet beam case, i.e., $h(t) \ge a + l$ in the third equation of (8). Since the dynamics of the flip-through phenomenon imposes a rapid change of the beam conditions from completely dry to fully wet (i.e., $a \le h(t) \le a + l$ in the third equation of (8)), a numerical solution is used here to solve the vibrational problem associated to each mode. To this purpose the solution for the vibrational potential vector is assumed of the form

$$\boldsymbol{\phi_v} = \sum_n \boldsymbol{A}_n \sin(2n+1)\pi \frac{y}{2h} \cosh(2n+1)\pi \frac{x+L}{2h} \tag{9}$$

which satisfies, in the BVP (8), the Laplace equation and the boundary conditions on the free-surface, the bottom and the wall opposite to the impact. This corresponds to using the Fourier Transform method, hence a linear system is solved for the unknown coefficients $\boldsymbol{A}_n$ which forces the fulfillment of the boundary condition on the tank side with the deformable beam. At each time t, $h(t)$ is measured from the corresponding experimental image.

The present solution of the potential vector has been validated against the results of a Higher Order Boundary Element Method (HOBEM) used to solve the BVP (8). In this case the BVP has been rewritten within an integral formulation using the Green's second identity; the integral equation is discretized by means of quadratic elements on the boundaries of the computational field.[8,9] The results of the comparison, limited to the modal analysis, are presented hereinafter.

D. Modal analysis: Structural natural frequencies

The equations of motion (7) with $p_r = 0$ are solved with the aim to determine the natural frequency of each mode of the beam. Since the added mass matrix is time dependent, a more and more complex solution of the homogeneous problem is achieved depending on the shape function assumed for $[A(t)]$. In the following, just to give a rough estimation of the wet natural frequency (under the hypothesis of a quasi-static variation of the wetted length), the added mass is assumed to be constant on the time scale of the natural frequency. From the physical point of view, this is equivalent to solve the BVP (8) with the free-surface flat and constant in time, i.e., frozen. Assuming the solution to be harmonic, that is $\boldsymbol{q}(t) = \boldsymbol{Q}e^{i\boldsymbol{\sigma_w}t}$, the homogeneous problem related to Eq. (7) gives the eigenvalue problem:

$$(\boldsymbol{\sigma_w}^2[M + A] - [K])\boldsymbol{Q} = 0. \tag{10}$$

The natural frequency vector $\boldsymbol{\sigma_w}$ is evaluated from the characteristic equation:

$$\det(\boldsymbol{\sigma_w}^2[M + A] - [K]) = 0. \tag{11}$$

When $[A] = 0$, the dry natural frequency vector is simply

$$\boldsymbol{\sigma_d}^2 = (\frac{\boldsymbol{e}}{l})^4 \frac{EI}{M_b}$$

with $\boldsymbol{e}$ the eigenvalue vector associated with the problem. Figure 2 shows the variation of the wet natural frequencies associated with the first and second (i.e., $i = 1, 2$ in figure) modes of the beam as function of the instantaneous dimensionless filling height of the tank. The lowest dry natural frequency of the beam $\sigma_d(i = 1) = \sigma_{d,1} = 1.575$ kHz is used to make the data dimensionless. The symbols represent the solution obtained by using the HOBEM method to solve the BVP (8) for the added mass calculation. While, the lines represent the solution obtained by using the shape function (9) for the vibrational potential function. Their good agreement confirms the reliability of the latter method, which is preferred in the following (because of its higher efficiency).

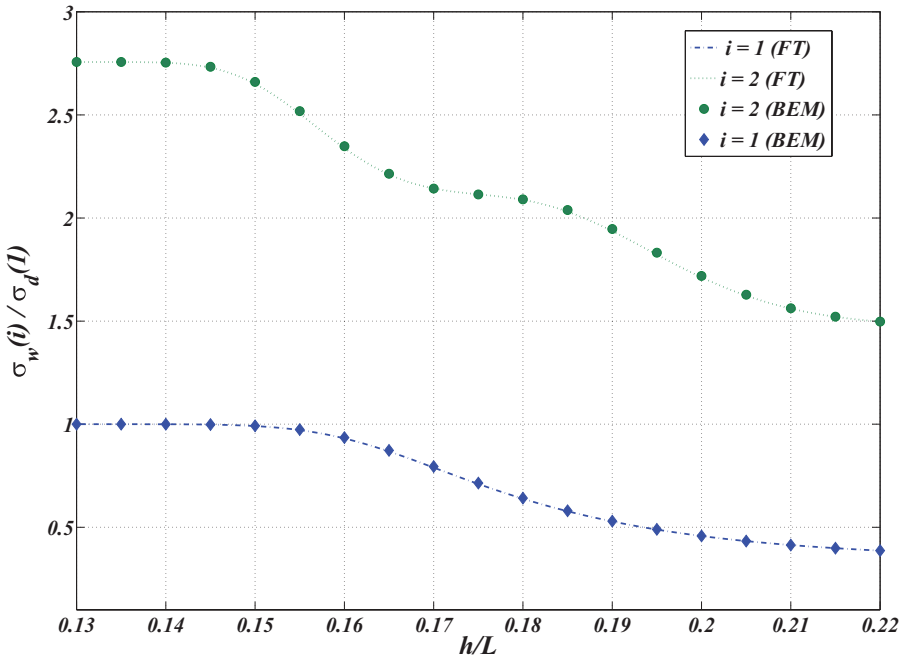

FIG. 2. Variation of the first (blue) and second (green) wet natural vibration frequency as a function of the filling depth. Symbols are obtained by using the HOBEM method, while lines come from use of the Fourier Transform method.

In the solution of the complete hybrid problem (i.e., with $p_r \neq 0$), although the free-surface is still considered flat at each time step, no hypothesis about the shape of the added mass function is given, since it is calculated from the solution of the BVP (8) by enforcing the instantaneous wetted length measured from the experiments. This means that $h(t)$ changes in time.

E. Scaling of the physical problem

The modal analysis is first used for the scaling of the experiment, in order to properly design the hydroelastic model which reproduces the behavior of the prototype. Sloshing model tests with hydroelastic impact require the simultaneous satisfaction of the Froude scaling together with proper scaling of the elastic properties of the structure.[7] Because of the complex structure characterizing a typical panel of a Mark III containment system, its complete structural scaling is an unresolved challenge, which is far from the aims of the present study. According to Faltinsen and Timokha,[7] we must ensure the Froude scaling of the relevant natural frequencies of the elastic vibrations of the structural panel. Further, Faltinsen and Timokha[7] showed that several natural modes play an important role in describing the maximum structural stresses in the Mark III panel and their frequencies vary between 100 Hz and 500 Hz. However, since the lower modes are associated with the steel plate of the Mark III panel, only the lowest is properly Froude scaled in the current investigation. In particular, for a LNG tank, whose typical length is about 30–40 m, the maximum length of a structural panel is about 3 m and the lowest wet natural frequency is around 110 Hz (in fully wet condition).[7] Because the sloshing tank used in the actual experiments is 1 m long (the same tank used in Refs. 4–6), a geometrical scale factor $\lambda = 30$ is assumed. This choice forced the length of the model beam to be equal to 0.09 m and the value of the lowest wet natural frequency (Froude scaled according to Eq. (3) and in fully wet condition) about 610 Hz. Using Eq. (11), such a frequency corresponds to the wet natural frequency of an aluminium beam with thickness 2.5 mm. Since previous investigations in rigid sloshing tanks[4–6] showed that the flip-through phenomenon occurs at a height of $h/L = 0.17 - 0.18$ from the bottom of the tank, an aluminium plate is placed with the lower end $0.13L$ above the tank bottom. Figure 2 shows that both the first ($i = 1$) and the second ($i = 2$) natural frequencies tend to decrease by increasing the filling depth; this is a consequence of the increasing added mass. A similar behavior is then expected also during the evolution of the flip-through as a consequence of the changing wetted length of the beam. However, they remain quite far from each other; this suggests that they remain uncoupled and justifies the scaling of the lowest mode of vibration only.

III. EXPERIMENTAL SET-UP

A 2D plexiglas tank ($L \times H \times B = 1$ m $\times$ 1 m $\times$ 0.1 m) reinforced with steel and aluminum structure (see Fig. 3) has been used. It is almost the same tank used in the previous experiments with rigid tank.[4,5] The difference is the presence of an aluminium plate on the lateral left wall (highlighted by the white arrow in the red oval in Figure 3).

The lateral left wall has been completely rebuilt in stainless steel (see right panel of Figure 4) and milled (see enlarged view on the bottom-left panel of Figure 4) to hold the deformable aluminium plate (see enlarged view on the top left panel of Fig. 4). A suitable clamping system has been designed (visible on the left panels of Figure 4) to ensure clamped conditions at the vertical ends of the plate. Conversely, its lateral boundaries have been left free and sealed with silicone.

The plate is 110 mm high. However, two bulges (each one 10 mm high) have been built at both vertical ends (see enlarged view on the top left panel of Fig. 4) to realize the clamping system. Then, the deformable part of the plate is extended vertically for 90 mm according to the geometric scaling specified in Sec. II E. Since the sloshing flows reproduced in the model tank and here studied are almost 2D, the deformable part of the plate behaves like a beam; then, its bending deformation is measured by means of 5 half-bridge strain gauges HBM $XY11 - 3/350$ placed along the centreline at 12, 28, 45, 62, 78 mm from the lowest end of the beam, i.e., at 142, 158, 175, 192, 208 mm from the bottom of the tank.

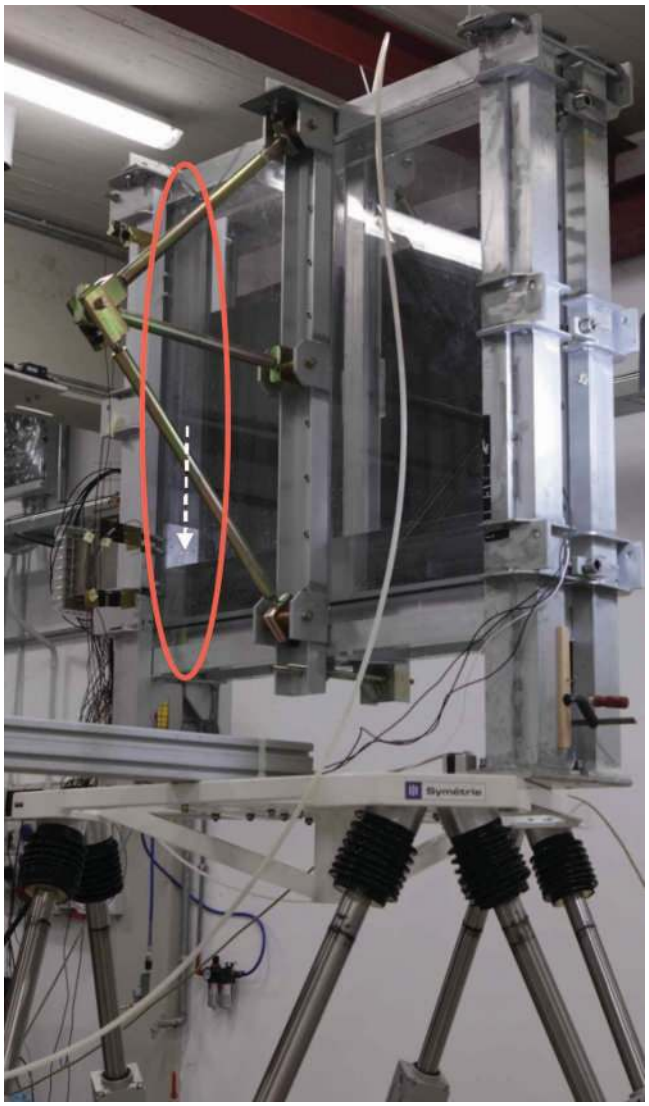

FIG. 3. View of the plexiglas tank reinforced with aluminium and steel structures. The red oval highlights the left lateral wall built in stainless steel and holding the deformable aluminium plate (indicated by the white arrow).

A. Static calibration of the strain gauges

The strain gauges have been calibrated by imposing uniform load along the clamped beam. In particular, once the plate has been mounted and clamped on the stainless steel wall, static tests have been performed by lowering the pressure inside the tank in order to reproduce uniform pressure distribution on the plate. The calibration factor of each gauge has been computed by comparing the measured strain with the theoretical solution given by the beam theory and with the numerical data obtained by using a finite element method (FEM)[19] on the 2*D* plate. Several pressure conditions inside the tank have been realized, in order to perform a linearization of the calibration factor. A linearization error lower than 2% has been measured for each strain gauge. Because of the half-bridge configuration used for the strain gauges, their output is proportional to the difference ($\epsilon_a - \epsilon_t$) between the axial and transversal strains. However, transversal strains can be assumed to be negligible during the sloshing tests performed in the present research investigation; nearly 2*D* flow conditions were realized during the whole experimental activity.

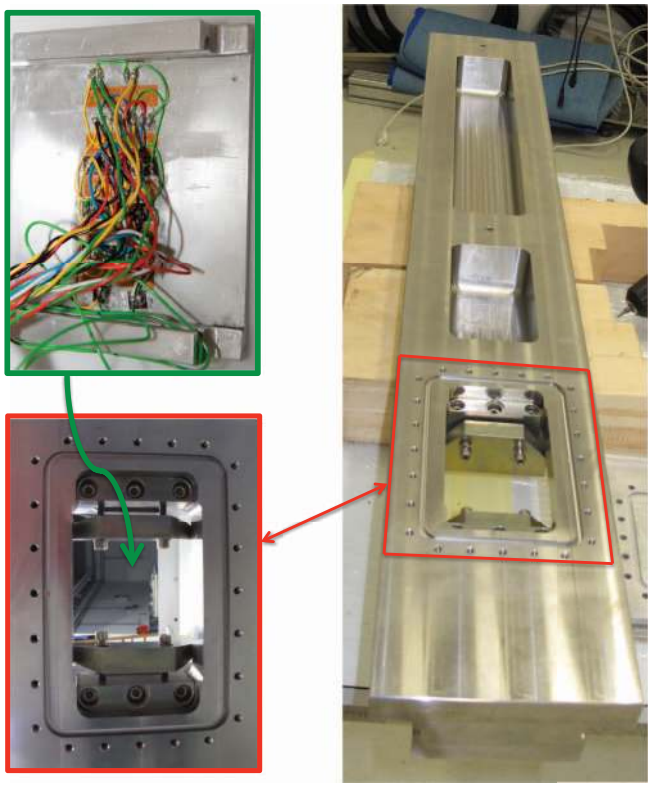

FIG. 4. Right column: Enlarged view of the external side of the stainless steel lateral wall, before being mounted on the tank. The red frame highlights the part milled to hold the aluminium plate. Bottom-left panel: Enlarged view of the external side of the milled part with the clamping system. The aluminium plate is mounted from the internal side. The screw holes around are not used in the present experiments. Top-left panel: Enlarged view of the aluminium plate with the full-bridge strain gauges along the vertical centreline. The bulges at both vertical ends are used to clamp the plate at the stainless steel wall.

B. Dynamic calibration of the strain gauges

Impulsive tests with a calibrated hammer have been also performed to check the dynamic behavior of the strain gauges. The hammer test consists in hitting the structure, hence giving an impulsive load which excites a wide frequency spectrum. Because the hammer is calibrated, the time history of the impulsive load can be recorded, as well as the response of the structure through the strain gauges. This allows both for a measurement of the dynamical response of the structure and for the dynamical response of the strain gauges. For the latter, a FEM method solving the structural problem on the same structure with the same input load is necessary. The hammer blow is given as close as possible to the centre of the plate. Due to the impulsive and intrinsically $3D$ load distribution (the tip of the hammer is small), the beam theory is no longer valid; the plate theory must be applied and transversal strains affect the measurement of the strain gauges. Figure 5 shows the comparison of the measured strains (symbol) along the plate with the numerical results of the FEM model ϵ_a applied on the $2D$ plate (continuous line) at the time of the maximum strain and for two different hammer tests. The maximum value of the impulsive load is reported at the top of each panel in Fig. 5. The small difference is justified by the contributions of the transversal strains ϵ_t, numerically evaluated and represented by the short-dashed (red) line in Fig. 5. This is due to the strongly $3D$ load applied. Since the global flow during the flip-through phenomenon studied here is $2D$, this difference does not affect the experimental results of the present investigation. The value $(\epsilon_a - \epsilon_t)$, calculated and indicated by the green line in Fig. 5, shows a good agreement with the corresponding experimental measurements, hence validating the adopted calibration procedure.

Use of the strain gauge to measure such an intense dynamics of the strain time evolution might be questionable. To further check the dynamic response of a single strain gauge, an accelerometer

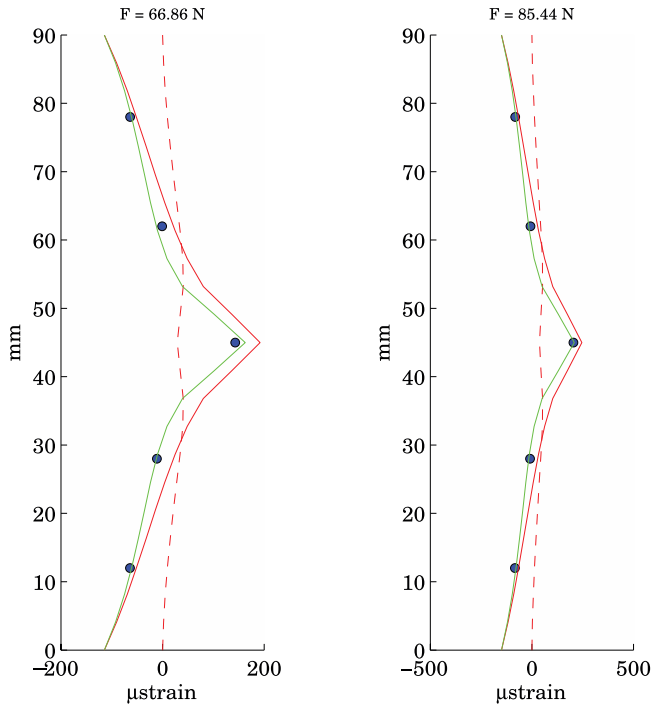

FIG. 5. Hammer test: Strain distribution along the centreline of the plate at the time of the maximum strain and for two different impulsive loads (whose maximum is indicated at the top of each panel). Symbols represent the measured strains along the vertical centerline of the plate, while the red continuous line reports the strains distribution ϵ_a predicted by applying a FEM method to the 2*D* plate. The short-dashed red line represents the transversal strains ϵ_t calculated numerically. Finally, the green dashed line gives the difference $\epsilon_a - \epsilon_t$.

has been mounted as close as possible to it at the same vertical position. An accelerometer is a transducer with a reliable response at high frequencies. Then, a hammer test has been performed and the time histories of the signals (acceleration and strain) have been compared in Fig. 6 (top panel) together with the corresponding logarithmic value of the amplitude (bottom panel) spectrum. They confirm the reliability of the strain gauge measurement, at least until 2.0 kHz. In the low frequency range (lower than 300 Hz) the strain gauge is a transducer with a reliable dynamic response; the disagreement with respect to the accelerometer is mainly due to the low energy content of the spectrum in that frequency range. Because of the limitation in the dynamic response of the strain gauges, hereinafter our analysis is mainly focused on the highest natural vibration period of the beam. As a consequence, each observation about the effects of the higher modes (whose frequencies are larger than 2.0 kHz, see Fig. 2) should be regarded purely qualitative.

Since the aim of the present work is the assessment of the hydroelastic effect during the wave impact in a LNG tank by means of the hybrid model proposed in Sec. II, the same slamming events have to be reproduced both in the case of the full rigid wall and for the wall with deformable plate. To this purpose, a second setup corresponding to the fully rigid case (no hydroelastic case) has been built to measure the pressure distribution along the rigid wall. The aluminium thin elastic plate has been replaced with a rigid 20 mm thick aluminium plate. Five differential pressure transducers Kulite (with full range equal to 38 kPa) have been mounted along it at the same position as the strain gauges in the elastic case. An accelerometer on the vertical stainless steel wall and a wire potentiometer are used to check the global horizontal motion of the tank. Two additional differential pressure probes have been installed on the stainless steel wall, below the removable plate (rigid or elastic). A filling depth $h/L = 0.122$ has been considered. The time evolution of all the transducer signals has been recorded at a sampling rate of 50 kHz. A high-speed camera with a rate of 5000 fps and a resolution of 1024 $\times$1024 pixels provided the visualization of the local flow during the evolution of the impact event while the global view of the sloshing flow in the tank has been recorded through two slow

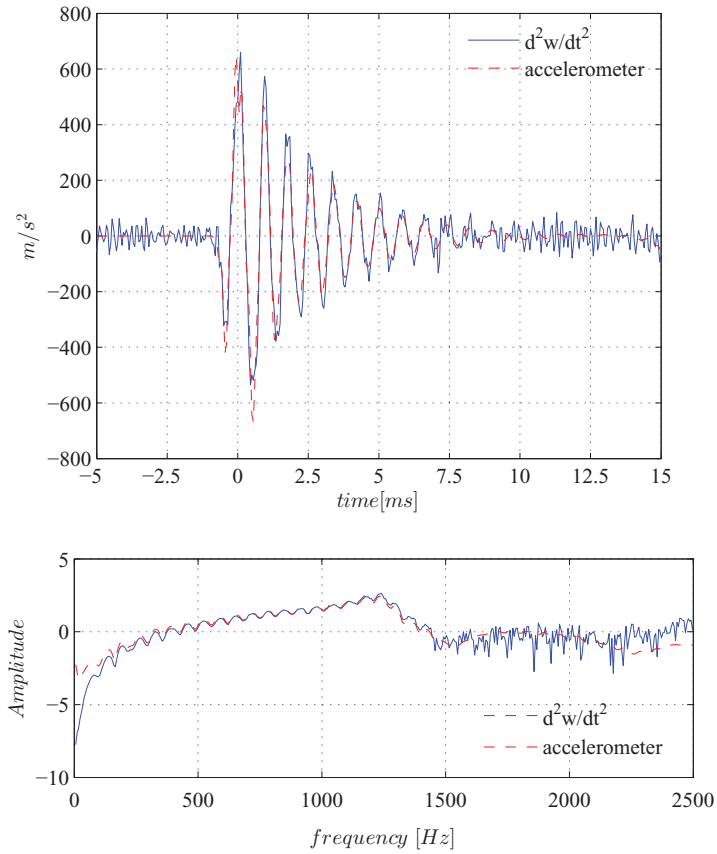

FIG. 6. Hammer test. (Top panel) Comparison between the acceleration time history on the plate measured through an accelerometer and a strain gauge. (Bottom panel) Comparison of the amplitude of the corresponding Fourier Transform.

digital cameras (with a frame rate of 100 fps). The spatial resolution of the high-speed camera gives a calibration factor of 7.8 pixels/mm, which ensures high accuracy in the measurement of the instantaneous height of the wave at the wall.

A common reference signal was used to synchronize the flow images and the analog signals of the transducers. An absolute pressure transducer measured the ullage pressure inside the tank.

The tank is forced to move along its longitudinal axis with the sinusoidal motion,

$$x = Acos(2\pi t/T(t))$$

through the system "MISTRAL," a dynamic hexapod for the motion of the tank following the 6DOF. A is the amplitude of the motion, while $T(t)$ is the period which varies with a ramp function between an initial value and the final value $T_0 = 1.6$ s. The high accuracy of the system ensured a good repeatability of the forced motion. To reproduce a flip-through phenomenon (FT), an amplitude $A/L = 0.03$ is enforced with the following ramp function:

$$T(t) = T_0 + (T_1 - T_0)e^{-\left(\frac{t}{T_a}\right)^2},$$

where $T_1 = 4$ s and $T_a = 0.05$ s. The considered flip-through event occurs at the third cycle of oscillation, after one first impact event, with air trapping which occurs on the opposite wall.

C. Dry and wet lowest vibration natural frequencies

The hammer test has been used to check the lowest vibration natural frequency of the beam with respect to the theoretical value. According to Eq. (11), the lowest natural frequency varies with

TABLE I. Dry natural frequencies associated with the first two bending and torsional modes.

	Beam theory (Hz)	FEM plate (Hz)	Experiments (Hz)
1st bending mode	1575	1653	1486
2nd bending mode	4343	4564	4318
1st torsional mode	...	1902	1791
2nd torsional mode	...	2922	2795

the wetted length of the beam. Then, several hammer tests have been performed by using several filling depths of the tank. Initially, dry vibration frequencies have been measured and compared with the corresponding values predicted by the beam theory and by the FEM model applied to the plate. The comparison, reported in Table I, shows a satisfactory agreement. The time history of the strains measured at the centre of the plate and the corresponding Fourier Transform for a hammer test in dry condition are shown in the left and right panel of Figure 7, respectively. In the latter the frequencies associated with the first two bending and torsional modes of the plate are also highlighted. Because of the constraints of the plate, the first bending mode prevails. This is confirmed also by the test carried out in wet condition, where the first bending mode is dominant. Inspection of Table I reveals that the measured frequency associated with the first bending mode is quite close to that predicted by the beam theory. The disagreement can be attributed to the additional mass induced by either the wire or the strain gauges (see Fig. 4). This quantity, estimated in few grams (5–7 g) is compatible with the difference in the value of the first bending frequency measured and predicted through the beam theory. Then, in our hybrid model we consider the mass of the beam increased by 7 g with respect to the nominal mass value, obtaining a predicted value of the first bending frequency equal to 1.499 kHz.

To further stress the good approximation given by the beam theory, Figure 8 shows the comparison between the calculated wet natural frequency (blue line) associated with the first bending mode of the beam and the corresponding value measured through the hammer tests (green symbols) for several filling depths of the tank.

D. Experimental analysis of the structural damping

From a theoretical point of view, two contributions may influence the response damping: the hydrodynamic damping due to the boundary layer flow and the structural damping. The former is taken to be negligible in sloshing flows. However, by studying the oscillation of an air pocket entrapped by a standing wave at the roof of a sloshing tank, Abrahamsen[1] found that the boundary layer damping in the water domain influences the decay of the pressure signal when the frequency associated with the bubble oscillation is much larger than the main natural frequency of the global sloshing flow. In our study, in spite of the high oscillation frequency of the elastic plate, the structural damping governs the decay of the measured strain. It means that the hydrodynamic contribution does not matter. Moreover, the flow field associated with the local problem is completely different in the present case from that considered in Ref. 1.

Impulsive tests have been used to calculate the structural damping. The hammer test, indeed, reproduces a free-vibration test, that is mathematically represented through the homogeneous equation associated with Eq. (7). For this the solution

$$q(t) = Q_0 \exp(-\xi \omega_n t) \exp(i \omega_n t)$$

holds, under the hypothesis of small dimensionless damping ξ and neglecting the vibration modes higher than the first one (whose natural pulsation is indicated by ω_n). Note that $\xi = C_{11}$, with C_{11} the first element of the damping matrix $[C]$. This solution, properly multiplied by the eigenfunction $\psi_1(y)$, is used to calculate the time history of the beam deformation and then of the strain at the centre of the beam. The best fitting with the measurement of the strain gauge #3 during the hammer test, allows achieving the damping value.

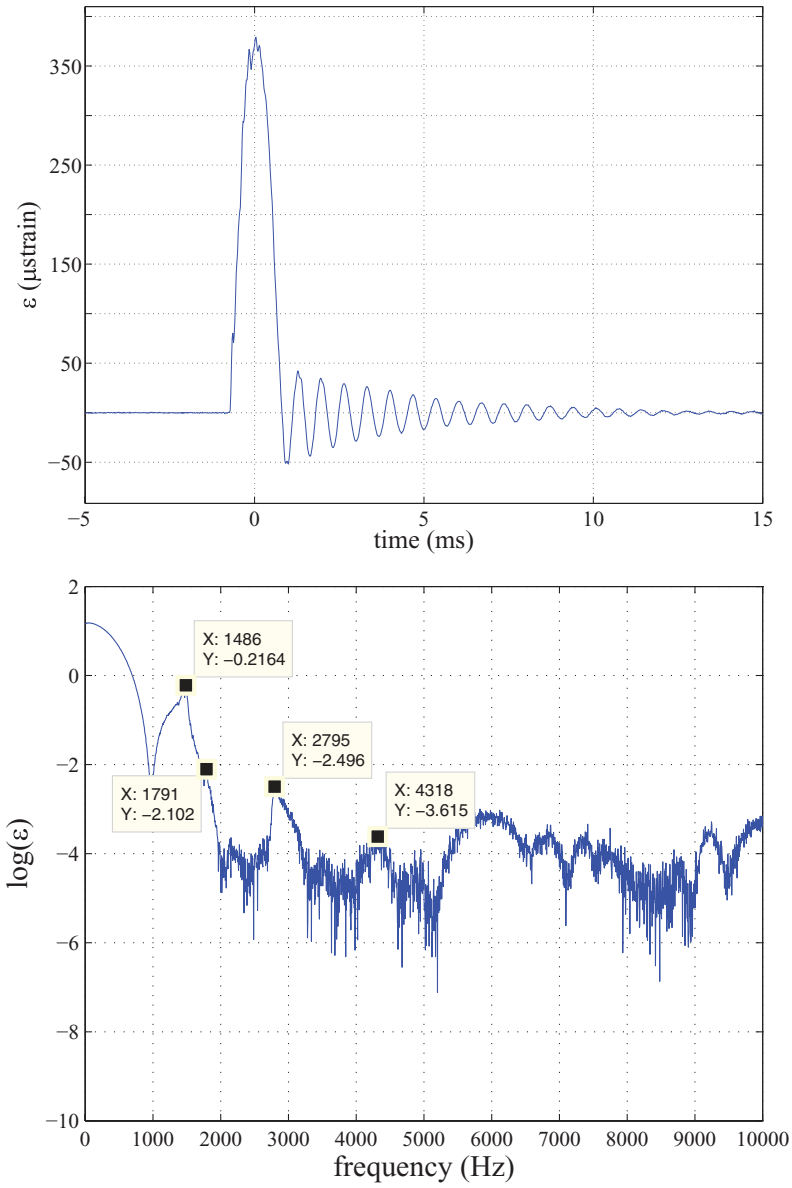

FIG. 7. Hammer test. Left panel: Time history of the strains measured by means of the strain gauge at the centre of the plate in dry condition. Right panel: Amplitude of the corresponding Fourier Transform. The frequencies associated with the first two bending and torsional modes are highlighted.

Structural damping is frequency dependent because of the varying natural frequency of the structure induced by the changing wet length of the beam. This implies that structural damping has been evaluated by performing free-vibration tests (i.e., hammer tests) with several filling depths of the tank, in order to realize several conditions of the elastic plate, from dry to fully wetted. A suitable constant damping value has been identified from each hammer test performed with a prescribed filling depth. Figure 9 shows the dimensionless damping coefficients relative to the lowest structural mode estimated experimentally as function of the filling depth. The dashed line illustrates the structural damping in dry conditions, while the symbol at $h/L = 0.13$ refers to the completely dry beam condition. The reported interpolation function (solid line in Figure 9) is used in the hybrid model to determine the dimensionless damping coefficient as a function of the beam wetted length.

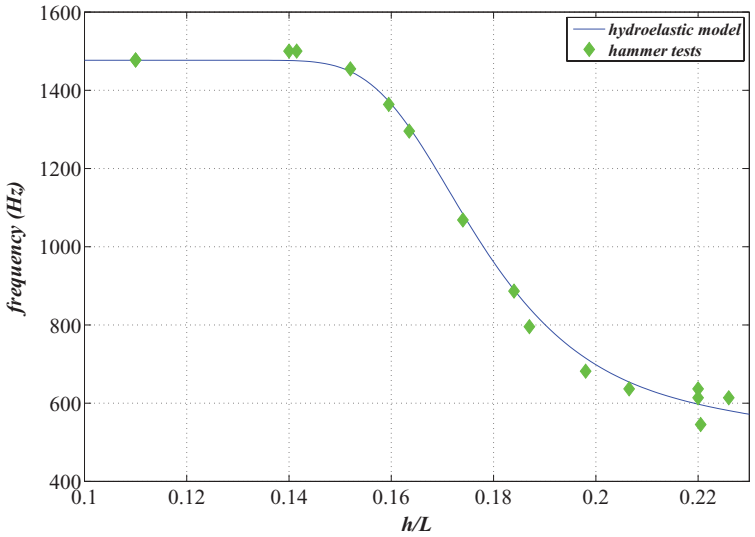

FIG. 8. Hammer tests in wet conditions: comparison between the measured natural frequency associated with the first bending moment (symbol) and the corresponding value predicted by the hydroelastic model (line) detailed in Sec. II, as function of the filling depth of the tank.

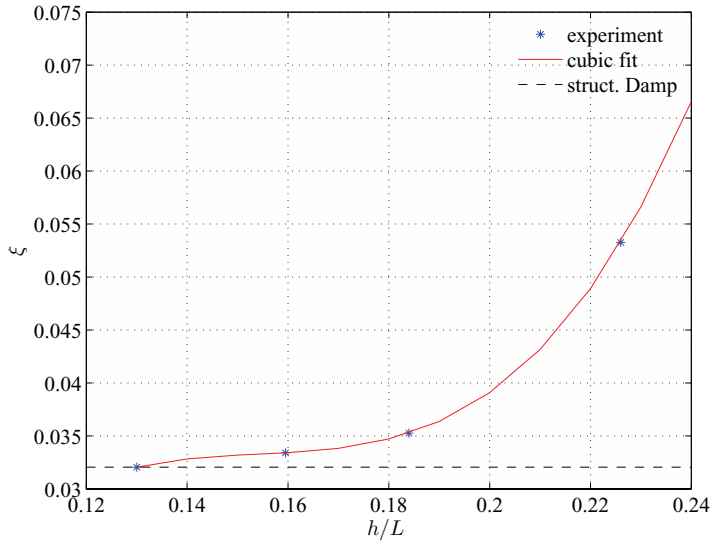

FIG. 9. Hammer tests in dry and wet conditions: dimensionless values of the structural experimental damping coefficient relative to the lowest structural mode (symbols). The solid line represents the cubic polynomial function which fits the symbols. The dashed line reports the values of the structural damping in dry conditions. $h/L = 0.13$ gives the completely dry beam condition.

IV. DISCUSSION OF THE RESULTS

A. Kinematic and dynamic flow fields

When a steep wave approaches a vertical wall, a flip-through event may occur causing large local loads.[12] The kinematic and dynamic evolution of a flip-through event along a rigid wall of a 2D sloshing tank is detailed in Ref. 6. Three different stages are recognized: (i) *wave advancement*, characterized by the wave front, moving towards the wall, which forces the wave trough to quickly rise up; (ii) *focusing* stage, where the wave crest and trough approach to one another causing their focusing and then the occurrence of the (iii) *flip-through*. The latter stage causes a sudden turning of the flow close to the focusing area which forces the formation of an energetic vertical jet. This

is associated with a rapid change of the contact angle between the free surface and the tank wall. Here we are considering a *pure* flip-through, i.e., with no air entrapped, but more generally in our previous studies[4–6] we demonstrated that the flip-through always occurs when a steep wave hits a wall, even when air is entrapped and it is associated with the formation of a jet flow escaping from an open cavity.

1. Rigid wall case

Figure 10 (Multimedia view) shows the evolution of the *pure* flip-through event generated along the rigid wall during the present experimental activity: each image shows the flow configuration for all the stages that characterize the wave impact. On each panel the vertical pressure distribution along the wall (red line) is also reported as reconstructed from the interpolation of the pressure signals recorded by five gauges P_3, P_4, P_5, P_6, and P_7 located on the rigid wall at the positions highlighted by the green diamonds. Two other gauges, P_1 and P_2, were placed at $y = 35$ and 50 mm from the bottom of the tank, respectively, but they are not shown in the figure.

The evolution of the local loads at the wall reflects the kinematic behavior of the flow field: the hydrodynamic term induced by the slow increase of the vertical velocity at the wall (see left panel of Fig. 11 in Ref. 6) added to the quasi-static term (i.e., to the term $\rho g(h(t) - y_i)$ where $h(t)$ is the instantaneous height of the wave trough at the wall and y_i the vertical position of the i_{th} pressure sensor) characterizes the local load distribution during the *wave advancement* stage. Because of the small vertical velocity of the wave trough, at the beginning of stage (i), the quasi-static hydrostatic pressure prevails, generating a spatial pressure distribution that decreases with the distance from the bottom of the tank down to zero at the free surface (see top-left panel in Figure 10 (Multimedia view)). This behavior is further confirmed by the time history of the pressure probes located along the wall and reported in Figure 11. In each panel, the dashed curve and the error bars represent the mean value of the pressure (made dimensionless with the hydrostatic pressure ρgh) and the corresponding standard deviation of five statistically equivalent repetitions of the same run, respectively. Moreover, the black line represents the result of a single run, i.e., that associated with the images of Figure 10 (Multimedia view). The time instants corresponding to the frames shown in Figure 10 (Multimedia view) are also indicated with the vertical dotted-dashed lines and highlighted through the labels *A, B, C, D,* and *E*, respectively. Each pressure signal refers to the atmospheric pressure, i.e., to a completely dry probe. The Euler equation,

$$\rho \frac{D\boldsymbol{v}}{Dt} = -\nabla p + \rho \boldsymbol{g}, \tag{12}$$

helps identifying the physical flow regime at each stage. Before and around the time of the first frame, i.e., $t = -10.0$ ms (labelled as *A* in Figure 11), $\frac{D\boldsymbol{v}}{Dt} \ll -\boldsymbol{g}$ meaning that the problem is dominated by the quasi-static term. The pressure signal of the probes below the instantaneous free surface increases almost linearly with the almost constant vertical wave velocity V according to the instantaneous quasi-static pressure $\rho g V t$ (see Lugni *et al.*[6]). To this purpose, the dashed line shown in the two panels of Figure 11, relative to the pressure at $y = 35$ mm and $y = 50$ mm, is drawn with the slope equal to the vertical velocity of the wave trough.

For increasing time within stage (i), the accelerating water along the wall causes an increase of the pressure signal recorded by the wetted probes, resulting in a nonlinear pressure variation in time (see Figure 11, around $t = -2.9$ ms labelled as *B*). Similarly, the spatial pressure distribution at $t = -2.9$ ms (top-right panel of Figure 10 (Multimedia view)) increases moving toward the free surface where the fluid velocity and acceleration are larger.

At the focusing time ($t = 0$ ms), the rapid increase of the vertical acceleration induces a strong and sudden growth of the $\rho \frac{D\boldsymbol{v}}{Dt}$ term in Eq. (12), which dominates the time and spatial evolution of the dynamic load. This causes an intense variation, both in time (see time range around label *C* in Figure 11) and space (see middle-left panel of Figure 10 (Multimedia view)), of the pressure signal, which reaches a maximum value (approximately equal to 10 times the undisturbed hydrostatic pressure) at the probe located at $y = 175$ mm above the bottom of the tank. At this time, see panel *C* of Figure 10 (Multimedia view), the pressure gradient can be roughly estimated as $\frac{1}{\rho}\frac{\partial p}{\partial y} \approx \frac{1}{1000}\frac{251000}{30.016} \approx 520$ m/s^2

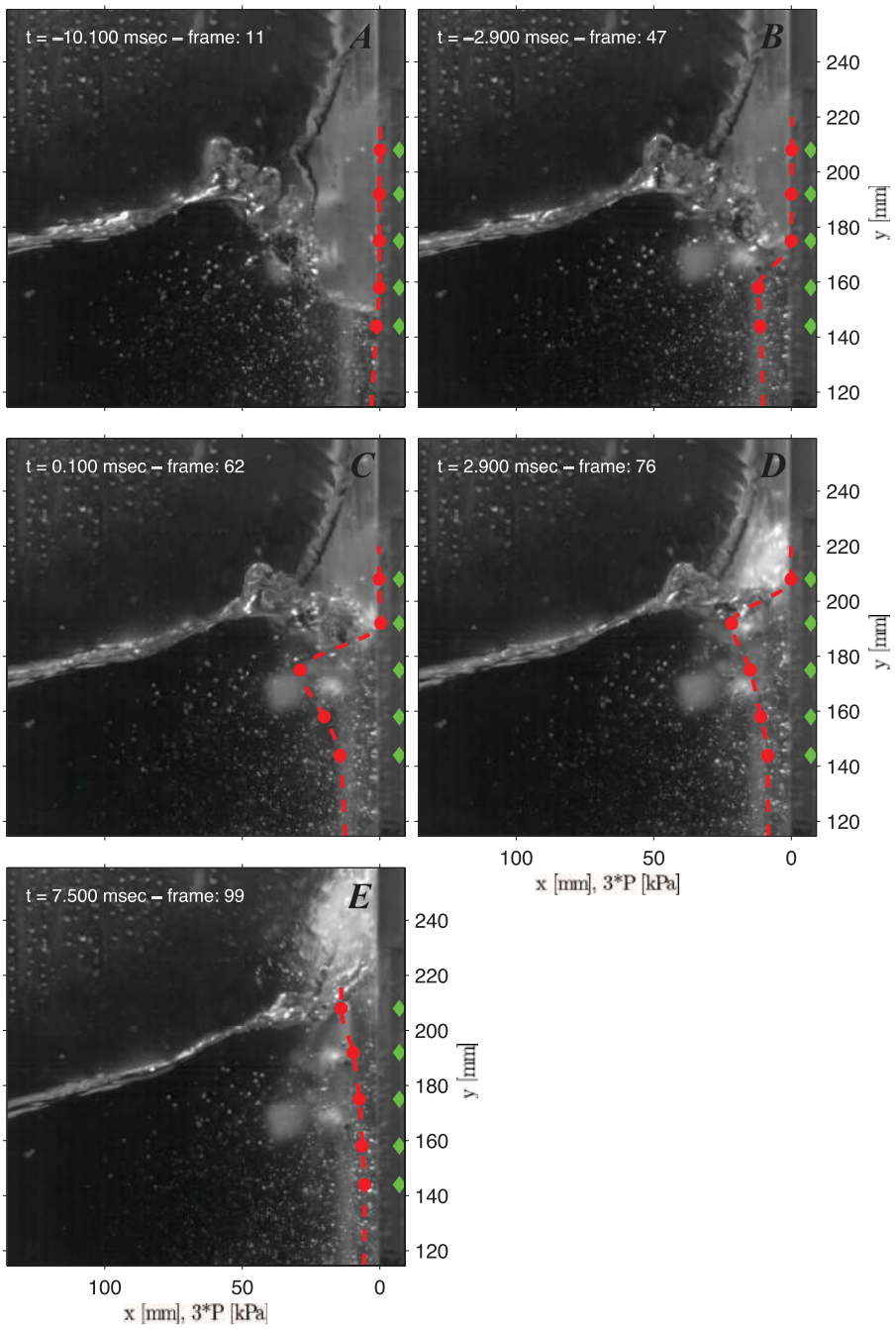

FIG. 10. Rigid case. Evolution of the flip-through event at five different times (reported on each panel). On each panel, the red dashed line represents the interpolation of the pressure data (red symbols) recorded by five transducers P_3, P_4, P_5, P_6, and P_7, numbered from the lowest position, placed on the rigid wall at the location indicated by the green diamond (Multimedia view) [URL: http://dx.doi.org/10.1063/1.4868878.1].

where 0.016 m is the distance between two subsequent pressure probes. This means that the vertical acceleration dominates over the gravity. At this stage, a jet flow is starting at the wall. The value of the jet acceleration estimated from the measured pressure gradient is lower than that given by the direct measurement of the acceleration shown in Ref. 6. This implies that a larger pressure value may occur between the pressure probes P_5 and P_6 at the time corresponding to panel *C* of Figure 10 (Multimedia view). A bias error must be accounted for when discussing this analysis where a single

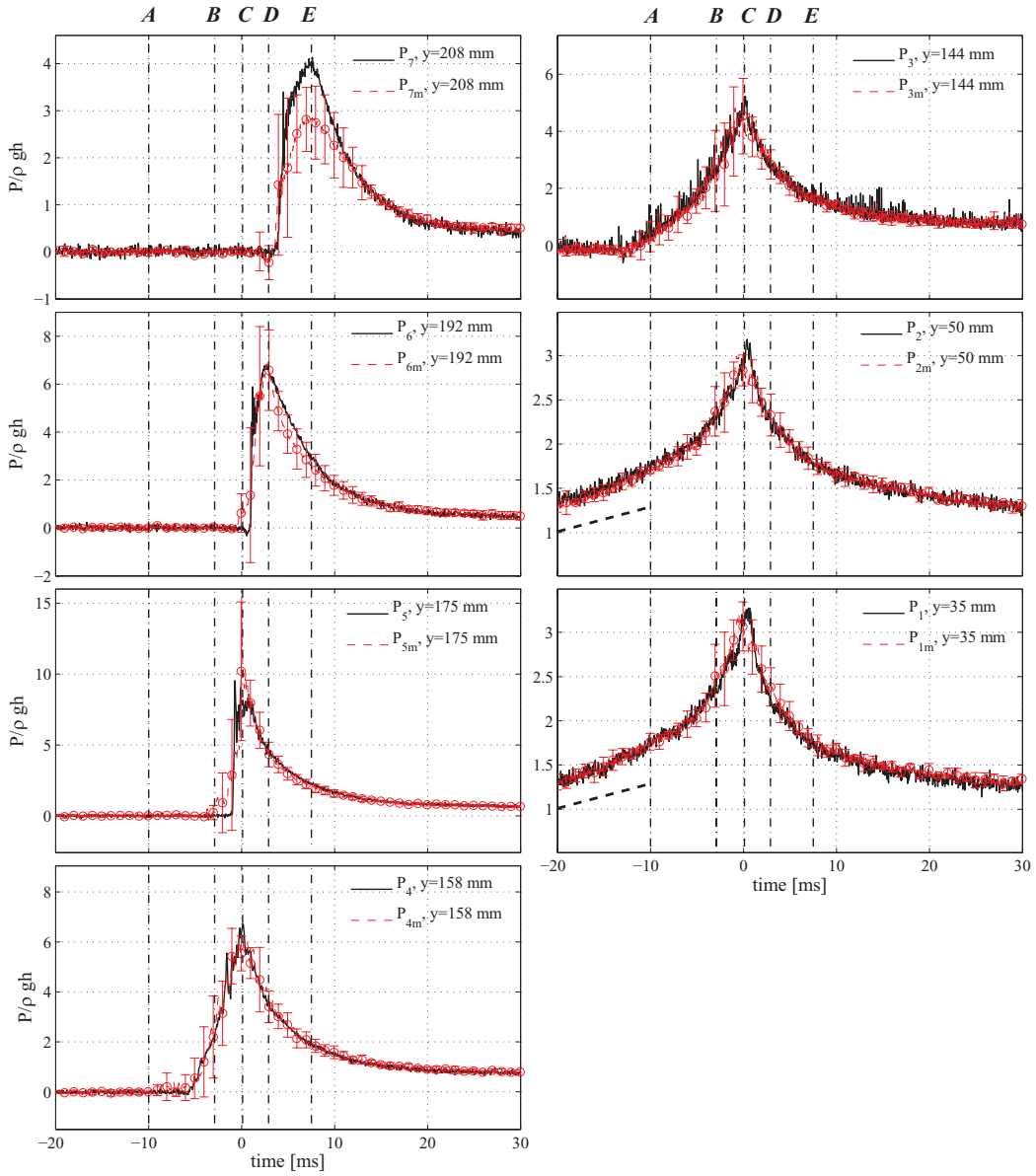

FIG. 11. Rigid case. Dynamic evolution of the flip-through event. Each panel reports the time history of the pressure transducers located at a prescribed position of the completely rigid vertical wall. The position is indicated on the panel. The red dashed line with symbols represents the mean value calculated with 5 repetitions of the same run; the related standard deviation is given by the error bar. The black line displays the data relative to a single run, i.e., that whose images are reported in Figure 10 (Multimedia view) and in the attached movie. The instants labelled as *A*, *B*, *C*, *D*, and *E* refer to times reported in the images of Figure 10 (Multimedia view). The slope of the black dashed line (present in the panels relative to P_1 and P_2 for $-20 \leq time(ms) \leq -10$) equals the vertical velocity V of the wave.

experimental run is examined. However, this error is assumed not to influence the results reported in Sec. V, where the mean value of the maximum load obtained from repeated runs is considered. Because of the highly local behavior of the pressure at the time of the impact, the standard deviation of the measured pressure takes into account the variability of the maximum pressure position also. From the kinematic evolution of Figure 10 (see middle-left panel *C*), the focusing area occurs at a location corresponding about to probe P_5; as a consequence, the transducers below this area show the maximum pressure peak at the same time and with a value decreasing with the distance from the focusing area. In contrast, the time histories recorded by the pressure sensors above P_5 shows a

time delay that is a consequence of the steadiness of the phenomenon in a reference system moving with the maximum pressure peak.[13] The latter moves upwards with a velocity approximately equal to the velocity V of the wave trough[6] (i.e., during the flip-through stage). During the focusing and the flip-through stages (see panels *C*, *D*, and *E* of Figure 10 (Multimedia view)) the vertical pressure gradients (varying between 520 m/s^2 in *C* and about 300 m/s^2 in *E*) govern the kinematic field giving the vertical acceleration of the flow. Because the last available pressure transducer is P_7 (panel *E*), the spatial pressure variation (red curve in Figure 10) stops here. However, for a rough estimate of the pressure gradients, we assume that pressure vanishes at the upper free surface, i.e., at $y \approx$ 225 mm from the bottom. The large pressure gradients are associated with the rapid turning of the flow around the focusing point. This type of pressure gradient is similar to the one observed at the spray roots during the water-entry phenomenon of a wedge. Since the beam portion above P_5 is dry during the previous stages (i) and (ii), the pressure signals recorded in (iii) above P_5 grow almost instantaneously from zero to the maximum value after a sudden drop (see Figure 11). Moreover, because of the disrupting jet occurring during stage (iii), the value of the maximum pressure peak above P_5 decreases with the distance of the pressure transducer from the focusing area (see *D* and *E* panels in Figure 10 (Multimedia view), and pressure sensor P_6 at the time labelled *D* and sensor P_7 at time *E* in Figure 11).

2. Deformable beam case

A rather different dynamic behavior is observed when a deformable plate is inserted in a rigid wall, rather than in a fully rigid wall. As discussed in Sec. II, the plate is assumed equivalent to a beam with the lowest wet natural frequency that is Froude scaled with respect to the corresponding frequency of a prototype panel of a LNG tank. The same motion of the tank used for the rigid case is applied to ensure the highest repeatability of the event. Five repetitions of the same run have been performed for the error analysis. Figures 12 and 13 show the flow behavior and the dynamic evolution of the local loads (stress and pressure, respectively) during several stages of the flip-through phenomenon. Each panel of Figure 12 (Multimedia view), beyond the image of the instantaneous configuration corresponding to the time specified, reports also the spatial deformation of the vertical plate through the dashed curve interpolating the values of the beam displacement (circle) measured at the strain-gauge positions (diamond). For a proper representation of the deformation curve, the local displacement of the beam is multiplied by a factor of 3×10^5.

Figure 13, from top to bottom, shows the time evolution of the dimensionless stresses (made dimensionless with the yield stress of the aluminium, i.e., $\sigma_Y = 15$ MPa) at three points along the centreline of the plate (i.e., at $y = 192$, 175, and 158 mm), and of the pressure measured on the rigid part of the vertical wall at a height $y = 35$ mm from the bottom of the tank. The dashed curve with the circles and the error bars represent, respectively, the mean value and the standard deviation of the physical quantity (i.e., stress or pressure) obtained through five repetitions of the same run. The solid line refers to the single run, whose evolution is shown by the images of Figure 12 (Multimedia view). The first six vertical dashed lines identify the times (from *A* to *F*) corresponding to the instantaneous configurations reported in Figure 12 (Multimedia view). The stress σ is calculated from the measured strain ϵ, using the relation $\sigma = E\epsilon$ with $E = 210$ MPa. The location of the pressure transducer is exactly the same used for the tests on the fully rigid wall.

The kinematic evolution of the flip-through event along the deformable beam resembles the one observed along the rigid wall (see Fig. 12 (Multimedia view)). The same three stages can be identified in the movie attached to the present paper. However, large differences characterize the dynamic evolution, especially after the focusing stage. Then, by referring to the dynamic evolution reported in Figure 13 the following regimes characterize the hydroelastic behavior of the beam during a flip-through event:

I. *quasi-static* regime, dominated by the quasi-static hydrodynamic load;
II. *fully hydroelastic* regime, characterized by the maximum stress distribution and by the strong coupling between the hydrodynamic load and the structural reaction;
III. *free-vibration* regime, where the structure behaves as a beam excited and free to oscillate.

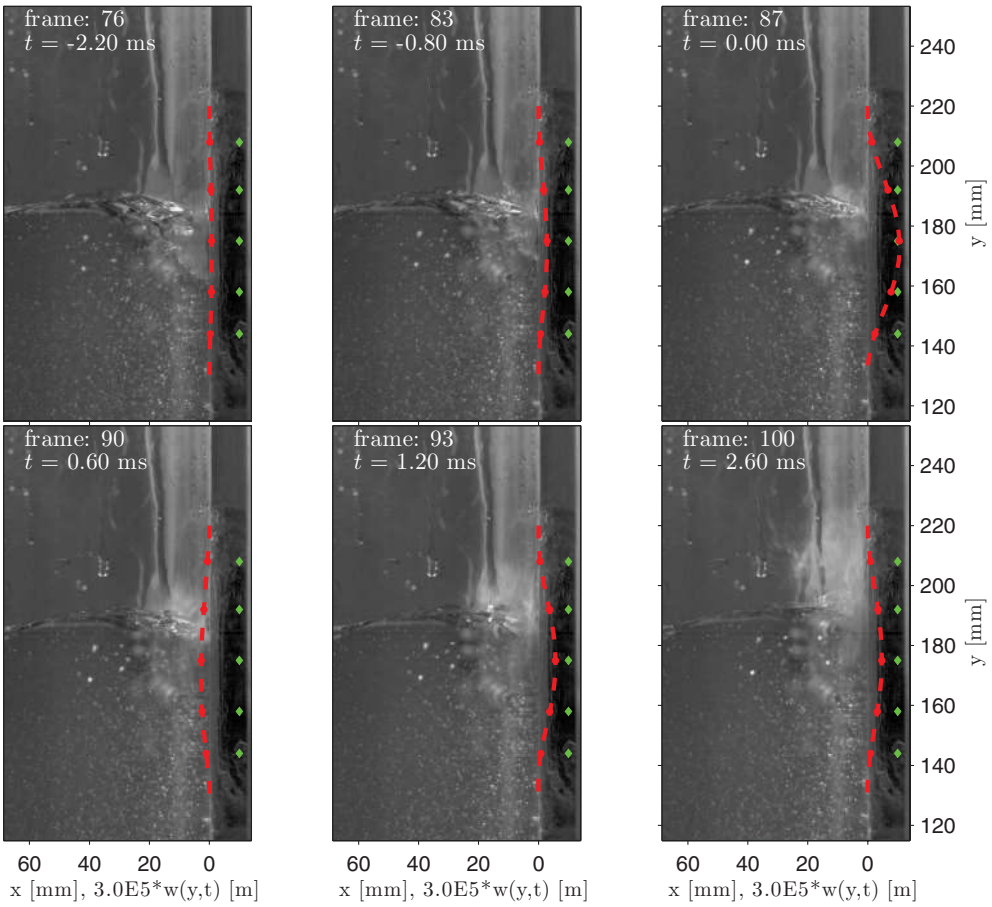

FIG. 12. Elastic case. Evolution of the flip-through event at six different times (reported on each panel). The red dashed line represents the interpolation of the beam deformation (red symbols) recorded through five gauges placed on the elastic wall at the location indicated by the green diamond (Multimedia view) [URL: http://dx.doi.org/10.1063/1.4868878.2].

During the *wave advancement* stage (top-left panel of Figure 12 (Multimedia view)), the quasi-static hydrodynamic load dominates, causing a weak and quasi-static deformation of the wall. This behavior characterizes the hydroelastic regime I in Figure 13, called *quasi-static*.

Evolving towards the *wave focusing* stage, the beam deforms smoothly (top-middle panel of Figure 12 (Multimedia view)). Because of the asymmetric load induced by the rise up of the trough, the second vibration mode of the beam matters at this stage. This is confirmed also by the different values of the stress loads measured by the sensors at $y = 158$ mm and $y = 192$ mm (see Fig. 13), i.e., placed symmetrically with respect to the centre of the beam at $y = 175$ mm. Starting from this time, the hydroelastic regime II called *fully hydroelastic* governs the dynamic evolution of the phenomenon (see Fig. 13) up to $t = 5$ ms.

At the focusing time $t = 0$ (see top-right panel of Figure 12 (Multimedia view)) the beam reaches its maximum deformation. Now, the first vibration mode of the plate dominates the spatial deformation field; however, from the evolution of the stresses (see the first three diagrams of Figure 13), the maximum value recorded at $t = 0$ ms is different at the strain gauges located at $y = 158$ mm and at $y = 192$ mm. This implies that the second vibration mode is relevant even at the focusing time, as a consequence of the asymmetric distribution of the wetted length of the beam.

The comparison of the pressure signal recorded at $y = 35$ mm for the rigid and elastic plate case (see Figure 14), emphasizes the role of the hydroelasticity. For each of them, both the average results (indicated with P_{1m}) and the instantaneous curve (indicated with P_1) related to the attached movies are also reported. Up to the focusing time $t = 0$ (identified by the vertical dashed-dotted line), both

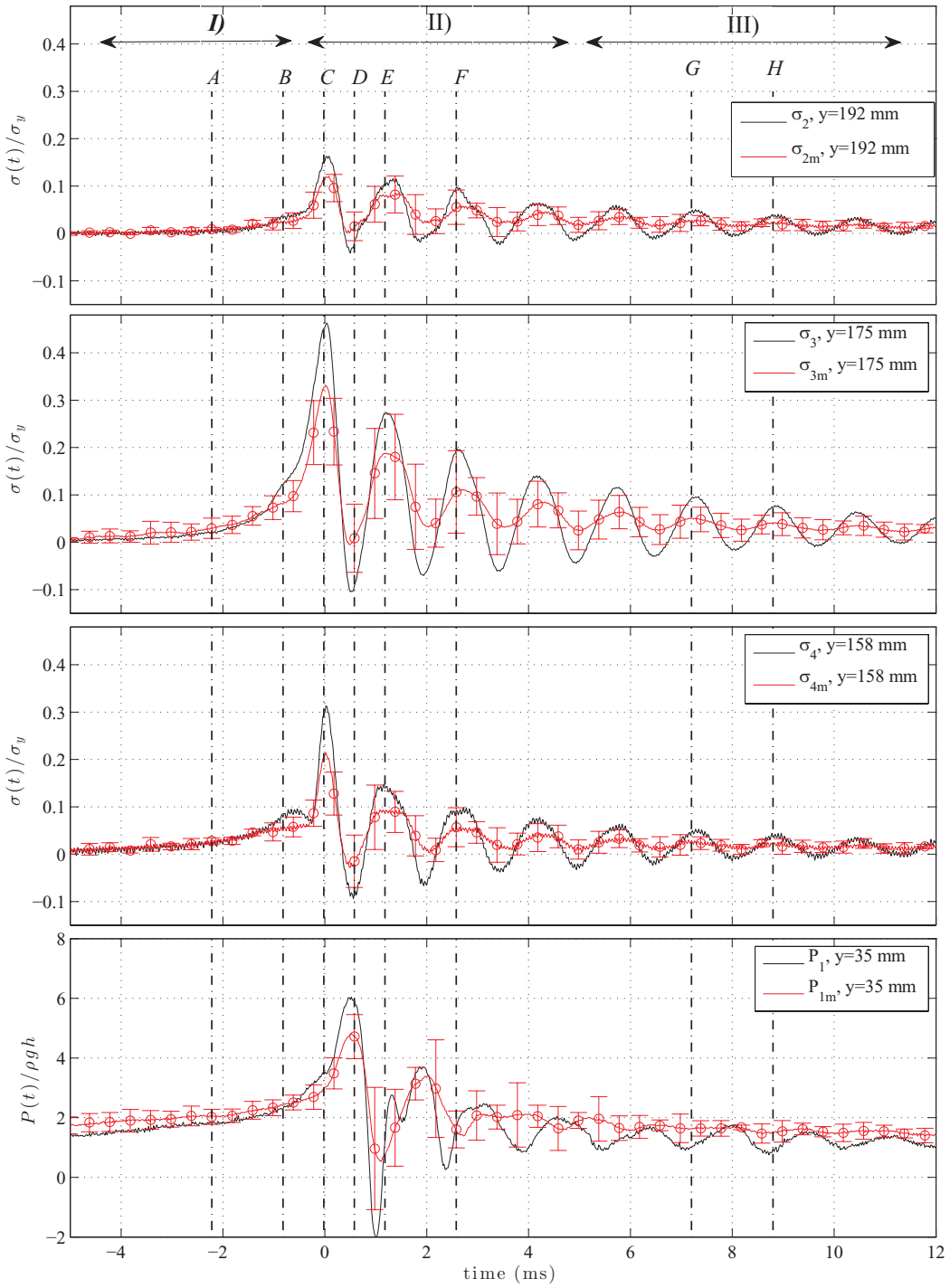

FIG. 13. Elastic case. Dynamic evolution of the flip-through event. From top to bottom, the first three panels report the time history of the strain gauges located along the elastic wall at the positions reported in the panel itself. The fourth panel reports the time history of the pressure transducer located at $y = 35$ mm above the tank bottom, along the rigid wall where the elastic plate is clamped. The red dashed line with symbols represents the mean value calculated with 5 repetitions of the same run; the related standard deviation is indicated by the error bar. The black line represents the data relative to a single run, that is the one whose images are reported in Figure 12.

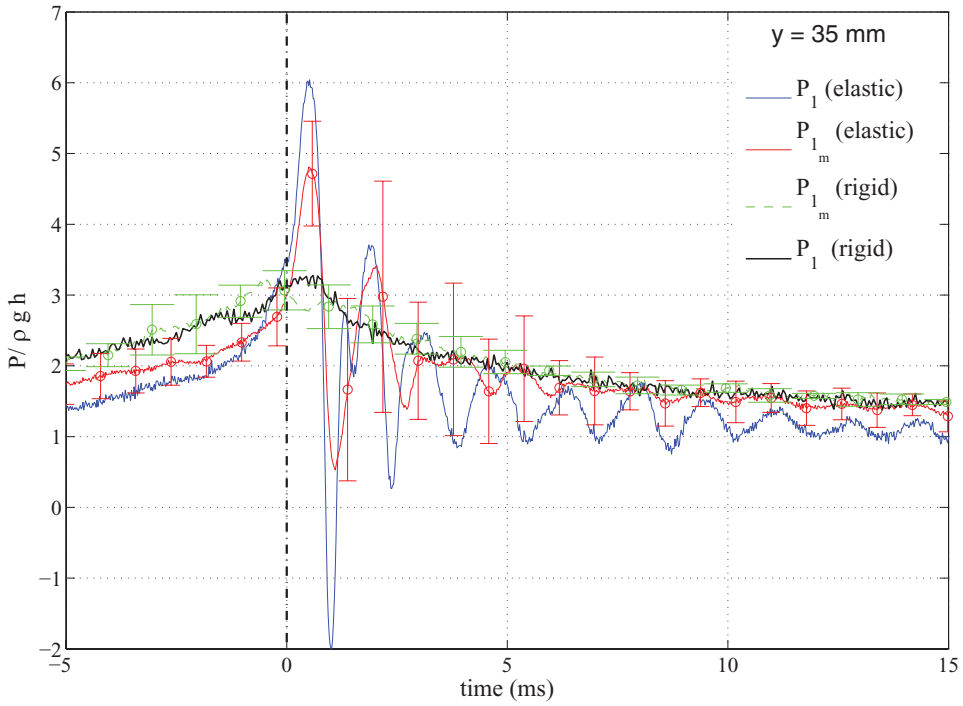

FIG. 14. Comparison of the pressure time histories measured at $y = 35$ mm above the tank bottom in the rigid and elastic case. For each case both the mean value with the relative error bar and the single run are shown.

signals appear similar, reaching the same value at $t = 0$. This means that the hydrodynamic forcing that originates from the focusing is the main cause of the maximum deformation of the wall.

In the following evolution of the phenomenon, a strong hydroelastic behavior occurs as illustrated by comparing the pressure signals in Figure 14. Due to the structural reaction, at the beginning of the *flip-through* stage, i.e., from $t = 0$ ms to $t = 0.6$ ms (the latter is labelled as D in Figure 13), the plate moves against the incoming wave, hence counteracting the hydrodynamic load (see panels C and D in Figure 12 (Multimedia view)). This behavior causes a steady increase of the pressure field (see bottom diagram of Figure 13) up to the maximum value at time D. The deflection field along the beam at this time reveals (see bottom-left panel of Figure 12 (Multimedia view)) that the second vibration mode is still acting. The maximum pressure measured at the sensor in $y = 35$ mm in the deformable plate case is twice the value measured in the rigid case (see Fig. 14), this revealing a strong hydroelastic effect. The full hydroelastic coupling persists for the next three oscillations of the signals (see bottom-middle and bottom-right panels of Figure 12 (Multimedia view), corresponding to times E and F in Figure 13), that is until $t = 6 - 7$ ms.

Later on, the beam behaves like a freely oscillating system, this characterizing the hydroelastic regime III (see Fig. 13) called *free-vibration*. The elastic plate is almost fully wetted, the first wet natural period of the beam is fully excited and governs the oscillation of the structure at this stage. Furthermore, for each oscillation cycle, the maximum stress measured on the elastic plate corresponds to a minimum of the pressure measured on the rigid wall below the deformable plate, and viceversa (see, for example, the times G and H in Figure 13). This behavior identifies the free-vibration regime of the beam which concludes the hydroelastic interaction.

B. Analysis by means of the empirical mode decomposition

The Empirical Mode Decomposition (EMD),[16] is a reliable mathematical tool to analyse the dynamic evolution of the local load at the wall, aiming to highlight the role of the hydroelasticity during the evolution of a flip-through event. Conversely, the classical Fourier Transform, assuming

the stationarity of the signal and giving the correct interpretation of linear problems, is inadequate for the comprehension of a strongly nonlinear and transient event like the flip-through.[5] Similar arguments are valid for the Morlet Wavelet analysis, being a Fourier based technique. The main idea of the EMD is the use of the Hilbert transform applied to a signal with (i) local symmetry around the local zero mean and (ii) the same number of zero crossings and extrema. Fulfilment of the previous constraints, allows for the definition of suitable basis functions, the Intrinsic Mode Functions (IMF), and ensures a correct application of the Hilbert Transform and, then, a meaningful definition of the instantaneous frequency.[5] The latter quantity is essential to understand the dynamic evolution of a transient nonlinear signal. Figure 15 shows the time evolution of the first three IMFs (top panel) obtained by the dimensionless stress signal σ_3/σ_Y measured at the centre of the beam, and the corresponding instantaneous frequency (bottom panel) colored as function of the local amplitude of the IMF. The theoretical variation of the first and second wet natural frequency, estimated through Eq. (11), are also represented with the dashed and solid line, respectively, in Figure 15. In Eq. (11) the wet natural frequencies depend on the wetted length of the beam. This has been measured at each time from the images collected by the high-speed camera. Because of the increasing wetted length of the beam, the added mass increases causing a decrease of the first wet natural frequency. The time variation of the dominant instantaneous frequency well reproduces the theoretical variation of the first natural wet frequency. The first IMF, reproducing the effect of the higher modes (in particular of the second mode), is almost zero at the centre of the beam, which is a node for the second

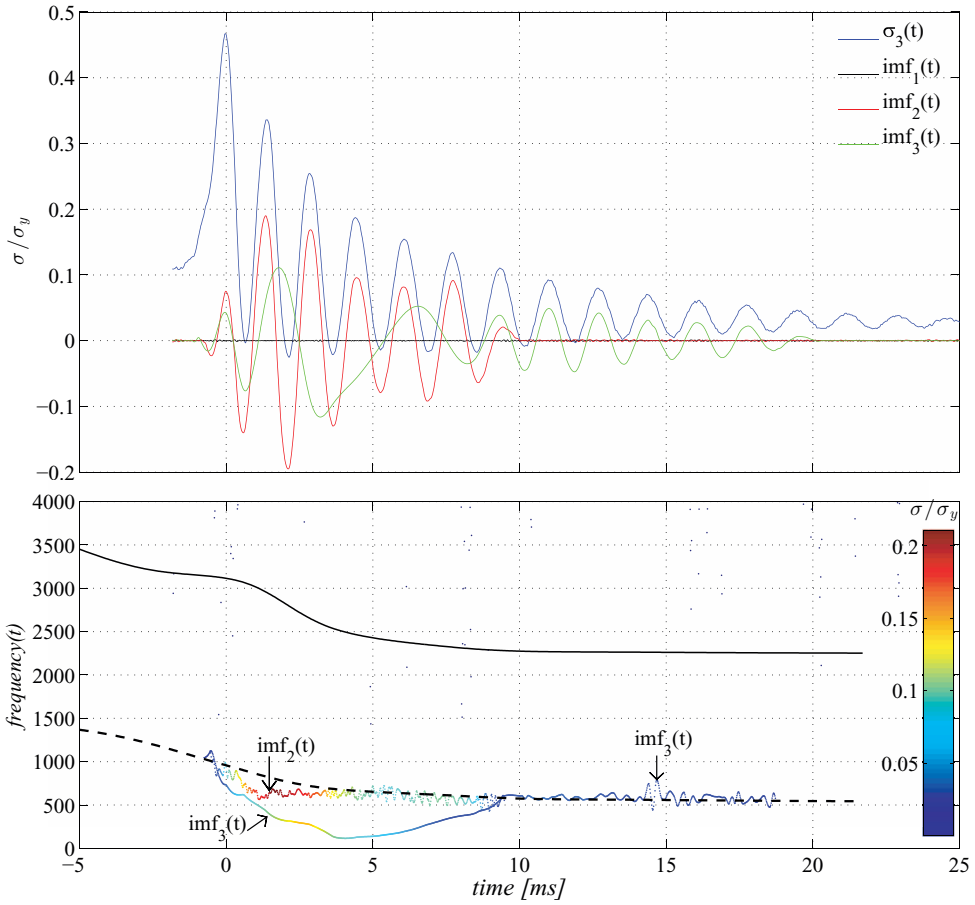

FIG. 15. Elastic case. Top panel: Time history of the stress measured at the centre of the beam and of the relative first three Intrinsic Mode Functions. Bottom panel: Time history of the instantaneous frequency associated with the three IMF reported above. Dashed and solid lines represent the theoretical variation of the first and second wet natural frequency of the beam, respectively.

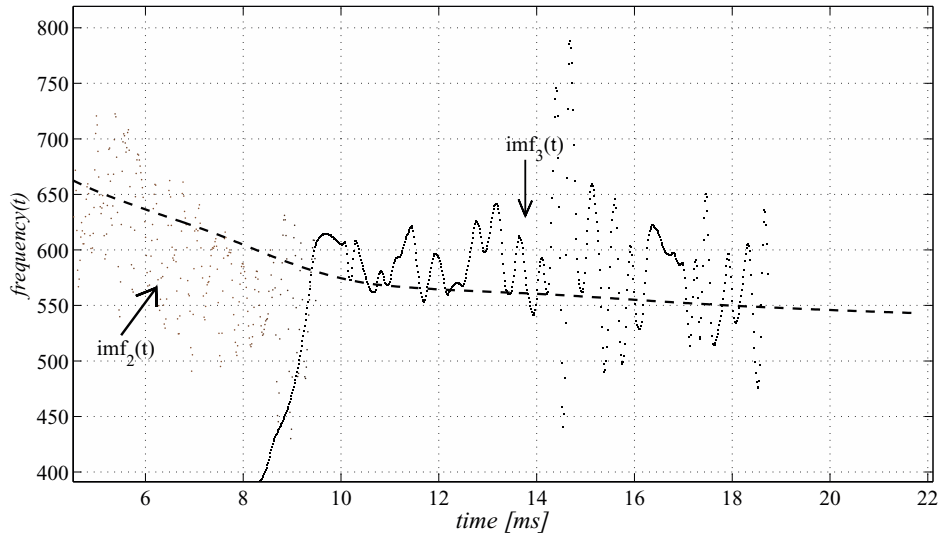

FIG. 16. Elastic case. Enlarged view of the instantaneous frequency reported in Figure 15.

mode. Conversely, the second IMF contains most of the signal associated with the dominant first wet natural frequency during the first six oscillation cycles. During the same time range, the third IMF modulates its instantaneous frequency from the first wet natural frequency around $t = 0$ ms to the changing value of the first wet natural frequency approximately at $t = 10$ ms. After this time, the third IMF contains all the energy of the signal associated with the free-vibration regime of the beam. However, over this time span the estimated theoretical frequency slightly decreases in time (as a consequence of the rising free-surface) while the experimental value remains almost constant. This aspect is emphasized by Figure 16 which shows an enlarged view of Figure 15. This difference, though small, is taken into account to improve the hybrid numerical model for times larger than $7 - 8$ ms.

The above considerations imply that during the hydroelastic regime II a quick variation of the added mass occurs; conversely, during regime III the added mass remains almost constant.

The strain gauge at the centre of the beam cannot capture the oscillations associated with the higher modes of vibration. To analyse the role of the second vibration mode, Figure 17 reports the time history of the first three IMFs derived from the stress measurements at gauges 2 and 4 (top panels), and the corresponding instantaneous frequency (bottom panels). It is worth to recall that the Froude scaling between prototype and model has been applied for the natural frequency associated with the first vibration mode only. Then, hereinafter, every observation about the second vibration mode is intended to be purely qualitative. As expected, the wet natural frequency associated with the second vibration mode has a marginal role and is limited to the time range around the first peak of the local load, i.e., the hydroelastic regime II and the beginning of regime III. This is confirmed by the time evolution of the first IMF in both the panels of Figure 17. The associated instantaneous frequency shows a large scattering of the data between the first (dashed line) and second (solid line) wet natural frequency of the beam. According to Faltinsen and Timokha,[7] the higher mode initially has an amplitude much lower than the lowest mode. Further, because of the relatively large damping, the higher modes nearly disappear at the scale of the period of the lowest mode. However, because of the dynamic response of the strain gauges used (see Sec. III) any quantitative evaluation of the energy associated with the higher modes cannot be expected.

V. COMPARISON WITH THEORETICAL MODELS

A. Hybrid model

In Sec. II we proposed a simplified hybrid model to investigate the role of hydroelasticity. Such a model takes into account both the pressure distribution measured in the corresponding experiments

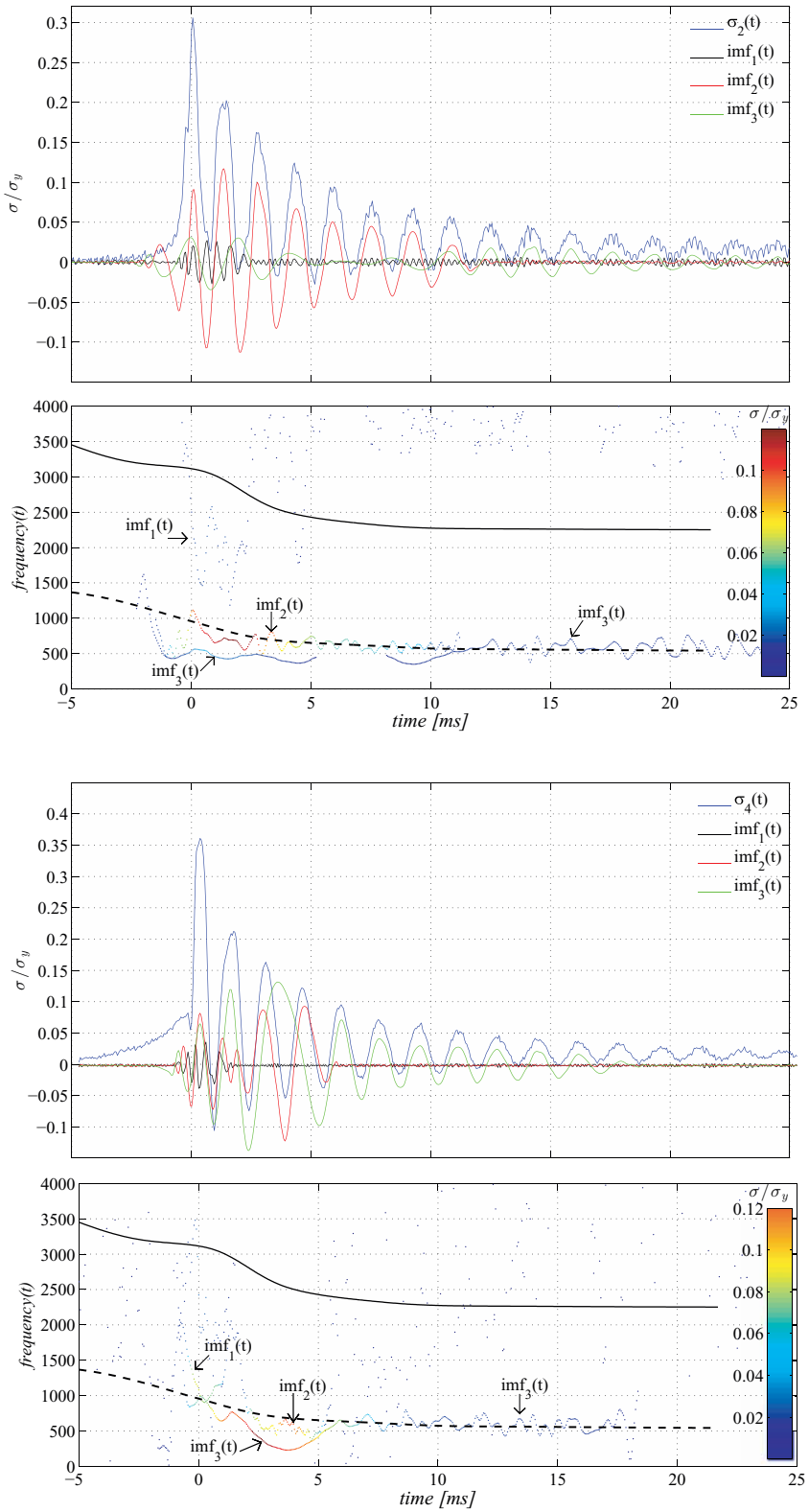

FIG. 17. Elastic case. First and third panels from top: time history of the stresses measured at the positions #2 and #4 and of the relative first three Intrinsic Mode Functions. Second and fourth panel: time history of the instantaneous frequency associated with the three IMF reported above. Dashed and solid lines represent the theoretical variation of the first and second wet natural frequency of the beam, respectively.

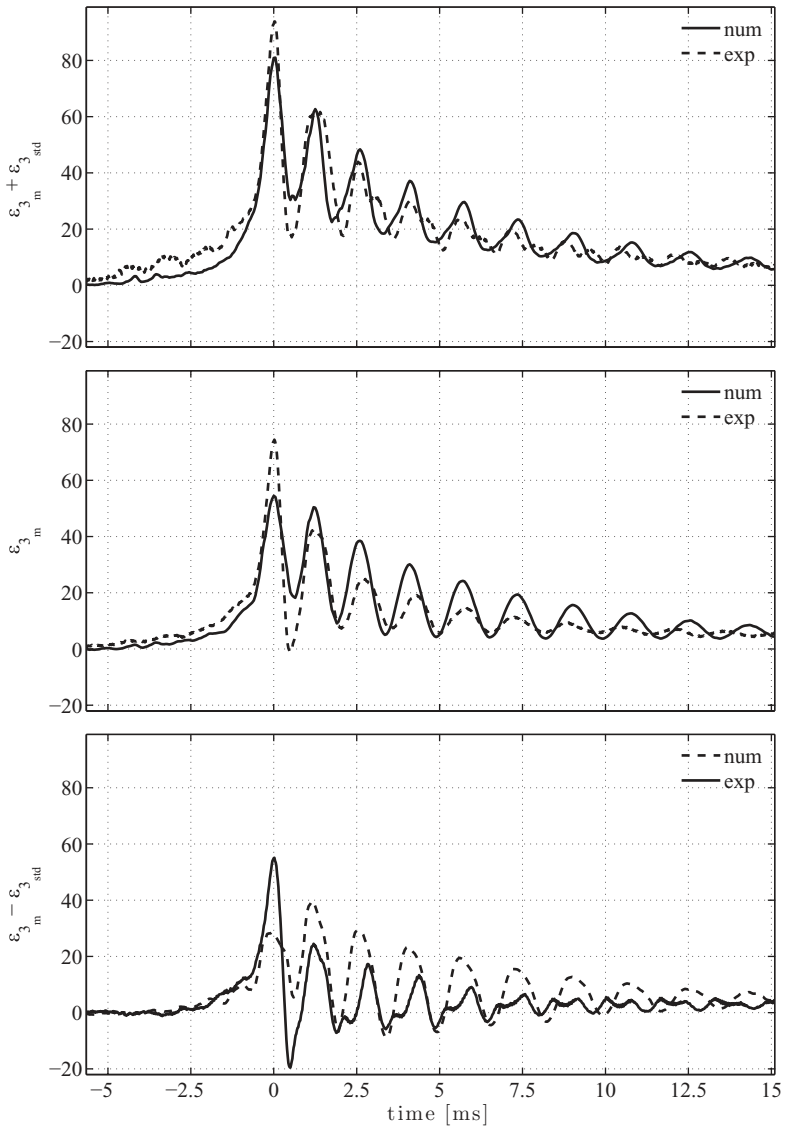

FIG. 18. Elastic case. Comparison between numerical prediction of the hybrid model (solid line) and experimental results (dashed line) relative to the time history of the strains at the centre of the beam. The mean value obtained by 5 repetitions of the same run (middle plot) and the corresponding value with added (top panel) and subtracted (bottom panel) the relative standard deviation, are reported.

on the rigid wall, and the time variation of the wetted length of the beam. This choice is a consequence of the experimental observations that highlighted the role of the quick change of the added mass induced by the changing wetted length of the beam. Figure 18 reports the comparison between the results of the hybrid model (solid line) with the data of the experiments (dashed line) for the time history of the strains measured at the centre of the beam. Five repetitions of the same run have been considered (both for the rigid case, used as input to the hybrid model, and for the hydroelastic case) to estimate the mean values (middle panel) and the maximum (i.e., standard deviation added to the mean value, shown in the top panel) and the minimum (i.e., standard deviation subtracted from the mean value shown in the bottom panel) variation. Both the structural and the hydrodynamic damping terms calculated in Sec. III D are used in the numerical results. At a first glance, the relative error, estimated as

$$Err\% = \frac{\epsilon_{3_{std}}}{\epsilon_{3_m}} * 100$$

with

$$\epsilon_3 = -\frac{t}{2}\frac{\partial^2 w(t, a + l/2)}{\partial y^2}$$

the strain at the centre of the beam and t the thickness of the beam, is larger for the numerical results ($Err\% = 41\%$) than for the experimental data ($Err\% = 25\%$), at least at the first peak ($t = 0$ ms in Figure 18). This behavior is a consequence of the larger standard deviation measured on the rigid wall experiments by using a pressure transducer. Conversely, on the elastic wall the repeatability of the measured strain is higher. The hybrid numerical solver is globally able to capture the wet vibration frequency of the beam at least for the first cycles of oscillation, i.e., until 6–7 ms in Figure 18; later a phase shift occurs.

With the aim to explain the disagreement between the theoretical model and the experiments for $t > 6$–7 ms, we recall the main assumptions of the hybrid model. In particular, the solution of (7) is based on the linear superposition of the forcing pressure field $p = p_r + p_v$. The first term accounts for the local hydrodynamic load acting on a fully rigid beam. Furthermore p_v, coming from the solution of the BVP (6) for the potential function ϕ_v, is used to calculate the added mass term $[A]$ in Eq. (7) associated with the vibrational problem of the elastic plate around a rest state. Since the solution of (7) depends on the instantaneous wet length of the elastic beam (through the boundary condition), the added mass will increase with $h(t)$. As a consequence, from Eq. (11), the wet natural frequency of the elastic beam will decrease by increasing $h(t)$. Even though this behavior justifies the ability of the hybrid model to properly capture the wet vibration frequency of the beam during the regime II, it cannot justify the phase shift between the numerics and the experiments occurring at $t > 7$ ms.

The hydrodynamic force can excite the structural reaction until the corresponding energy is larger than a threshold value. This threshold value corresponds, in the present case, to the fully wet beam and occurs at $t = 7$ ms (see Figures 15 and 16). When the energy content of the forcing contribute is insufficient, the structure behaves as a beam in the free-vibration regime,[7] i.e., it keeps vibrating with the frequency corresponding to the fully wet beam (this identifies the hydroelastic regime III). The latter is slightly larger than the frequency corresponding to the instantaneous filling depth (see also Figure 16) but it justifies the phase shift between the numerical solution and the experiments.

Because of the large scatter induced by the pressure measurements on the rigid wall and to better evaluate the capability of the hybrid numerical solver, the numerical results obtained using the maximum pressure distribution measured at the rigid wall are compared with the experimental data corresponding to the maximum strain distribution measured at the elastic wall. Even though the numerical results shown in Figure 18 account for the proper modelling of the damping term, in the following the effect of the damping term is analysed.

Figure 19, therefore, shows the comparison between the experiments (magenta line) and the numerical results (black line) calculated with no damping term included and with the added mass varying in time according to the instantaneous variation of the wet length. A reasonable agreement is observed for the prediction of the first peak. However, a difference of about 15% still persists. This means that further hydroelastic effects, not included in the present model, could matter at the first peak. As already observed, a good prediction of the instantaneous hydroelastic frequency exists as long as the beam is not fully wet. Later, i.e., for $t > 6 - 7$ ms, a time-dependent phase delay appears because of an unreliable estimate of the added mass in the numerical model (see Figure 16), as already mentioned above. Further, due to the absence of the damping term in the numerical model, prediction of the successive peaks completely fails. To overcome the disagreement, a suitable modelling of the physical damping is essential. Damping sources of the structural response are viscous dissipation, acoustic radiation damping, thermodynamic dissipation, and structural damping. The latter contribution is expected to be dominant in the present case. In Sec. III D the structural damping was assumed to be frequency dependent as a consequence of the varying wet natural period of the beam with its wet length. The damping coefficient has been determined by using the results of the hammer tests in dry and wet conditions; Figure 9 reports this dimensionless damping coefficient as a function of the dimensionless water depth of the tank. To assess the frequency dependence

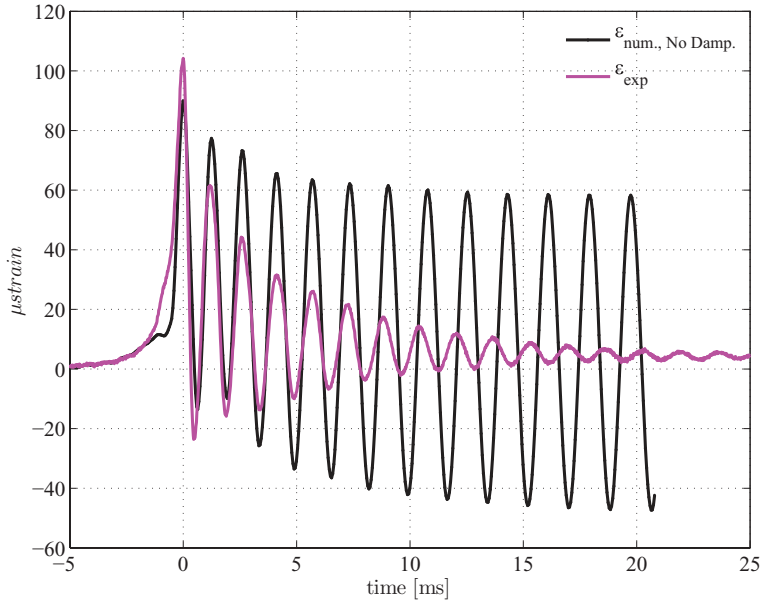

FIG. 19. Elastic case. Comparison between numerical prediction of the hybrid model (black line) without the damping term and experimental results (magenta line) relative to the time history of the strains at the centre of the beam. Both data are related to the run corresponding to the maximum measured value.

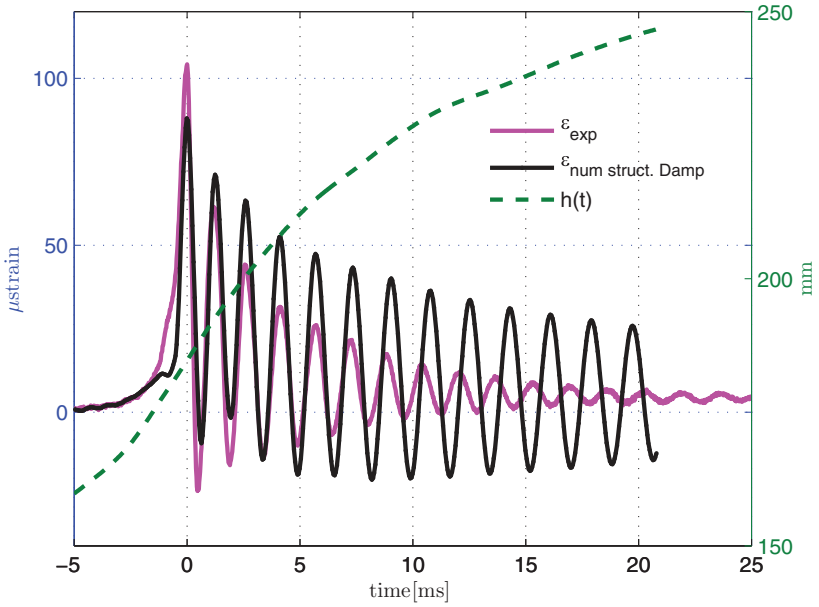

FIG. 20. Elastic case. Comparison between numerical prediction of the hybrid model (black line) with the constant value of the damping coefficient (evaluated in dry condition) and experimental results (magenta line) relative to the time history of the strains at the centre of the beam. Both data are related to the run corresponding to the maximum measured value.

of the structural damping, this is the first assumed constant in the hybrid model and it is taken equal to the value measured in dry condition (dashed line in Figure 9); the comparison between numerical results and experimental data related to the strain gauge #3 is shown in Figure 20. The time history of the wet length, used for the calculation of the added mass term, is also reported (dashed green line). Accounting for the structural damping in dry condition is not enough to justify the experimentally observed decay. The frequency dependent damping coefficient in wet condition (solid line in Figure 9) is then used; the results are shown in Figure 21. The green dashed line shows

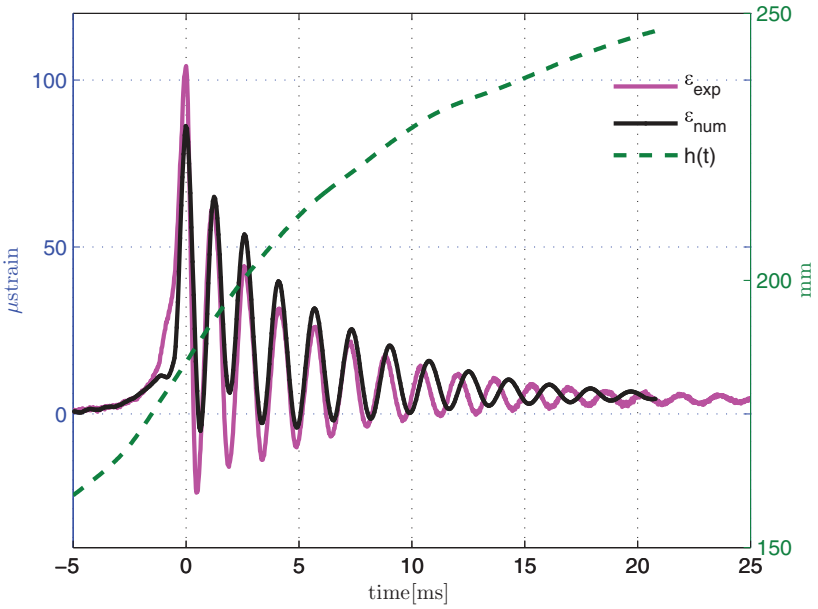

FIG. 21. Elastic case. Comparison between numerical prediction of the hybrid model (black line) with the varying damping term (evaluated as a function of the instantaneous wetted length of the beam) and experimental results (magenta line) relative to the time history of the strains at the centre of the beam. Both data are related to the run corresponding to the maximum measured value.

the instantaneous variation of the wet length which has been considered both for the calculation of the added mass and of the damping term (by using the results of Figure 9 solid line). Although the method used to estimate the damping coefficients does not completely account for the dynamic variation of the wet length of the beam, the agreement between numerical and experimental results is globally satisfactory. However, some differences appear in the first two-three oscillations (see Figure 21) after the first maximum peak, and more in general during the hydroelastic regime II. They are essentially related to the decay of the pressure time history measured in the fully rigid case (see Figure 11). In the proposed hybrid model the peak of the pressure distribution measured in the rigid case causes an impulsive load on the structure, which begins to oscillate as in a free-vibration regime (but with a varying natural frequency due to the changing wetted length). The disagreement between the results of the hybrid model and the experimental data in the prediction of the maximum amplitudes of the structural deformation of the elastic beam indicate that a stronger hydroelastic effect occurs during the first two/three oscillations of the structure, suggesting the need of a more reliable model for the regime II. At following times, i.e., at $t > 6 - 7$ ms, the hydroelastic evolution resembles the free-vibration behavior with a constant added mass. This means that a constant value of the wet natural frequency of the beam follows as detailed at the beginning of this section. To this purpose, Figure 22 shows the comparison of the numerical and experimental time histories of the strain at sensor #3 with the results of the numerical model properly enhanced with the constant added mass for $t > 6 - 7$ ms (i.e., a constant wet length, see green dashed line in Figure 22), resulting in a good agreement both in phase and amplitude.

B. Simplified models

A first question arises about the effectiveness of the mathematical models used during the design stage. Two different models are typically suggested by the classification rules to take into account the liquid-structure interaction: (i) FEA and (ii) Indirect Dynamic FEA. Method (i) solves the unsteady structural problem with the external forcing coming from the rigid pressure distribution measured in the sloshing model tests. In contrast, method (ii) solves the quasi-static FEA with forcing given by the maximum rigid pressure loads measured in the model tests. A suitable DAF which depends on the rise time of the local load, amplifies the calculated local stresses to

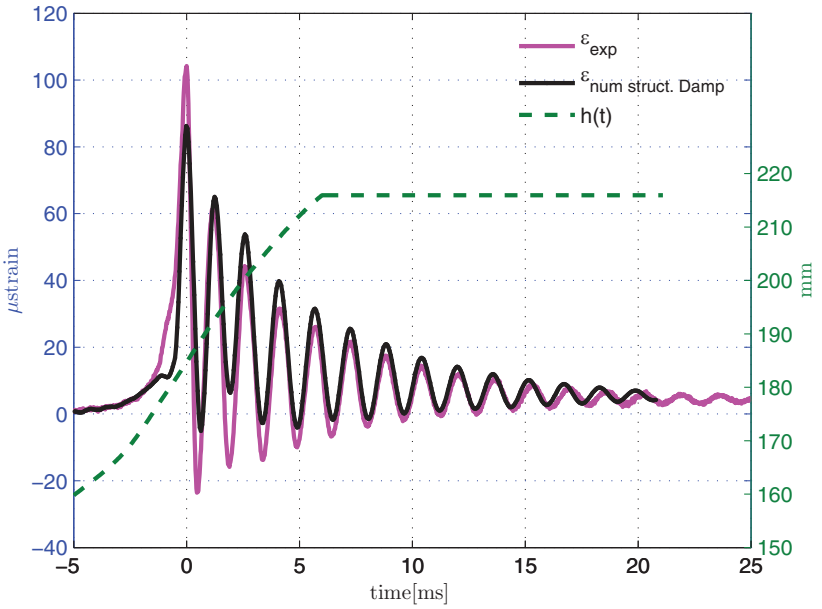

FIG. 22. Elastic case. Comparison between numerical prediction of the hybrid model (black line) with the varying damping term (evaluated as a function of the instantaneous wetted length of the beam) up to the fully wet condition (and then kept constant) and experimental results (magenta line) relative to the time history of the strains at the centre of the beam. Both data are related to the run corresponding to the maximum measured value.

account for the dynamic effects. Moreover, the proper modelling of the added mass term associated to the vibration of the structure is questionable. In the classification notes[10] it is suggested to calculate the added mass in model (i) using a linearized potential flow solver on a significant portion of the possible wetted surface of the membrane; however, the added mass is assumed to be constant in time. In method (ii) the DAF should take into account also the added mass contribution. To better understand the limits of the simplified methods, we implemented both models for the specific problem, and we compared their results with the experimental data for the elastic wall. In particular, method (i) resembles the hybrid method we proposed previously, except for the estimate of the added mass. In method (i) the added mass is kept always constant and estimated on an *a priori* prescribed portion of the wetted surface. Conversely, in the hybrid model the added mass is varying in time during the rise up of the wave trough along the wall (influencing the maximum peak of the structural load), and until the end of the focusing stage; after, when the jet is formed and the elastic wall is almost fully wet, the added mass in kept constant.

The comparison with the experimental results for the time history of the strains recorded by sensor #3 is shown in Figure 23. No damping term is used in the model. Although the first peak value looks similar to that estimated through the hybrid model, it occurs at a slightly different time. Furthermore, large differences characterize the evolution of the phenomenon. Due to the constant added mass used, the prediction of the vibration frequency completely fails. However, if the main interest is the value of the maximum load peak, method (i), consistently with the hybrid model, still underestimates the experimental value (around 20% lower than the experimental value). Nevertheless, this underestimation is much lower than that obtained from the quasi-static model, i.e., method (ii). In this model, Eq. (7) is applied by completely neglecting the inertial and damping terms; the pressure distribution is given from the measurements on the rigid wall experiments. The results, concerning the average and the corresponding error bar (calculated through the repetition of 5 runs) of the strain distribution along the vertical beam, are shown in Figure 24. Both the experiments (red symbol) with the reconstruction based on the use of the first natural vibration mode of the beam (red line) and the quasi-static calculations (blue symbol) are reported. Also for the latter, only the first vibration mode is used. Comparing the maximum value of the strain, the ratio between the measured strain and the quasi-static one, follows, i.e., $DAF = 1.84$. This value

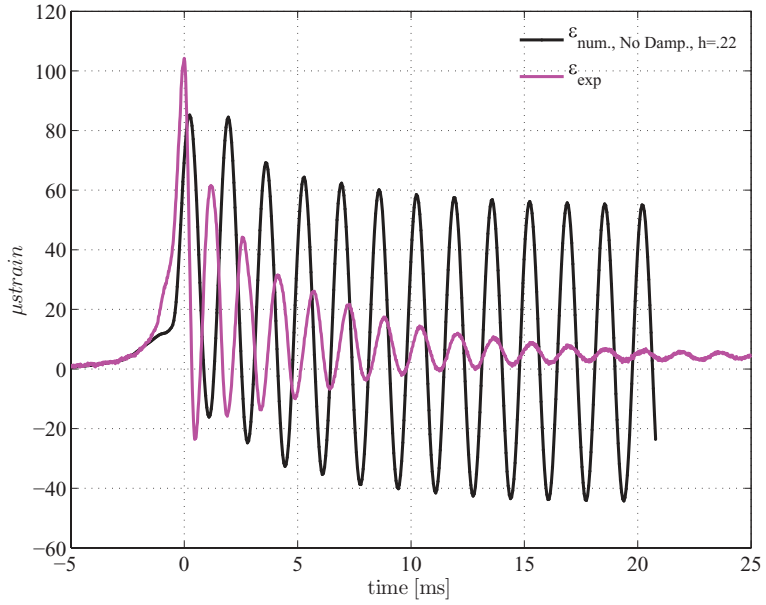

FIG. 23. Elastic case. Comparison between numerical prediction of the simplified model (black line) (i) without damping term, and experimental results (magenta line) relative to the time history of the strains at the centre of the beam. Both data are related to the run corresponding to the maximum measured value.

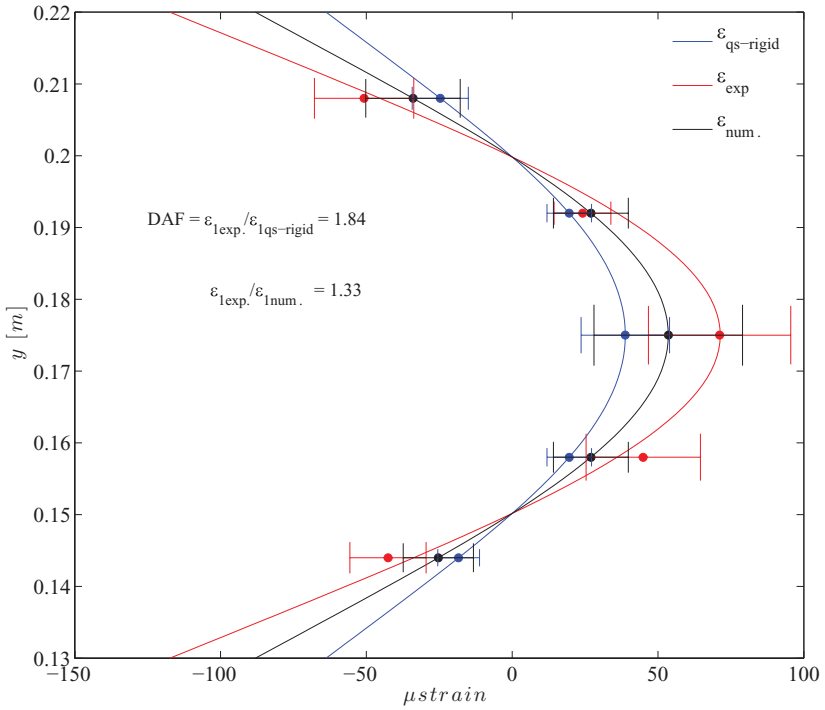

FIG. 24. Elastic case. Comparison between numerical prediction of the simplified model (i) (black symbol), of the simplified model (ii) (blue symbol), and experimental results (red symbol) relative to the mean value (with the error bar) of the maximum strain distribution along the elastic beam. The corresponding solid lines represent the strain reconstructions by using the first vibration mode of the beam.

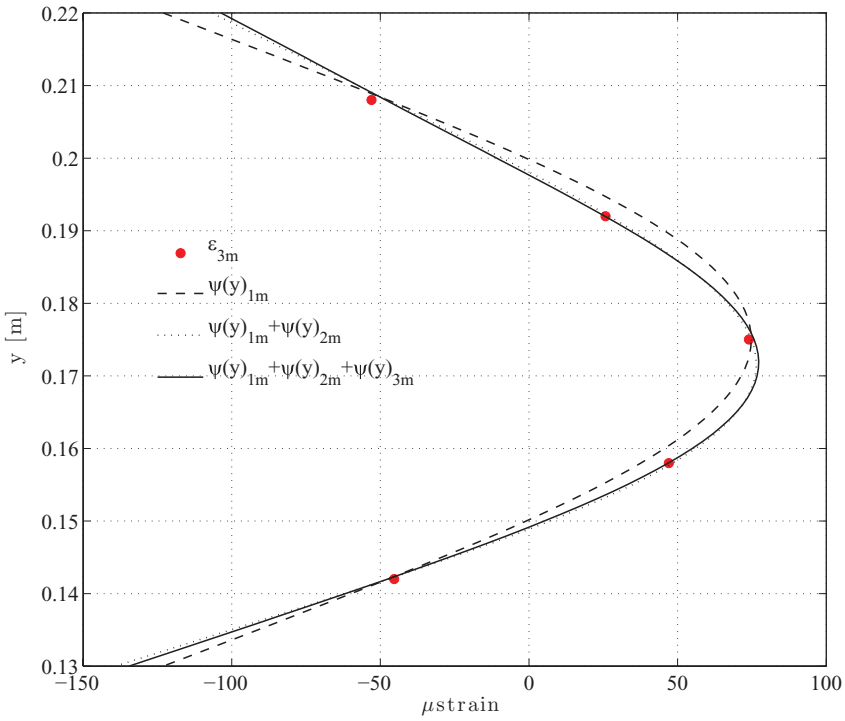

FIG. 25. Elastic case. Red symbols: experimental results relative to the mean value of the maximum strain distribution along the elastic beam. The corresponding strain reconstruction by using one (dashed line), two (dotted line), and three (solid line) modes is also reported.

is much larger than that proposed in Gervaise *et al.*[18] (approximately equal to 1 at the rise time measured in the present experiments, i.e., 1 ms at model scale corresponding to $5 - 6$ ms at full scale) using the dynamic model described in Pillon *et al.*[17] and applied to a Mark III containment system. However, in the present experiments a completely different type of impact and a different material for the structural panel is considered. Nevertheless, some remarks can be done. The model proposed by Pillon *et al.*[17] does not seem to account for the added mass contribution: a finite element method on a structural panel excited through the pressure load distribution measured during experiments on a rigid tank (with a well refined grid of sensors) is used. This aspect can explain why in Refs. 18 and 17 a maximum $DAF = 1.6$ is obtained at a rise time around 1 ms in full scale; a maximum DAF value at a larger rise time is expected when the added mass contribution is also considered. A third curve, the black one shown in Figure 24, is numerically obtained by using the simplified method (i) with the constant added mass term. In this case, a ratio between the experimental and the numerical maximum strain equal to 1.33 is achieved, confirming the essential role of the added mass in the dynamic calculation. Finally, the error bars reported on the data shown in Figure 24 allow to assess the reliability of the maximum strain (or stress) recorded at the centre of the beam. The experimental value on the elastic beam shows a relative error around 27%. Differently, the relative errors corresponding to the quasi-static and dynamic numerical model (based on the experimental maximum pressure value recorded at the centre of the beam in the rigid case) are around 42% and 48%, respectively. This confirms that the maximum strain (or stress) can be a good candidate to be used as an indicator of the maximum local load.

The mean value of the experimental maximum strain distribution along the wall reported in Figure 24 (red symbols), shows an evident asymmetric trend, even highlighted by comparing with the symmetric reconstruction using only the first vibrational mode (see red solid line in Figure 24). This behavior of the experimental data hides the effect of the higher vibrational modes. Their contribution to the local structural load has been previously discussed and observed at the time instant of the maximum strain. Figure 25 shows the experimental strain distribution (dot symbol)

and the related reconstruction using one, two, and three modes (dashed, dotted, and solid line, respectively), and assesses the role of the higher mode at this time. The first two vibration modes well recover the experimental measures of the strain along the elastic beam; the third mode is almost negligible. The maximum strain occurs at $y = 0.17$ m, i.e., 5 mm below the location of the strain gauge (in the elastic case) and of the pressure transducer (in the rigid case). This suggests the optimal positioning of the transducers (both for the rigid and elastic case) to be used in a next step of the study.

VI. CONCLUSIONS

A comprehensive experimental investigation has been carried out to explore and quantify the role of the hydroelasticity during the evolution of a flip-through event[6] inside a sloshing tank in low filling depth condition. A deformable aluminium plate, whose dimensions have been fixed in order to ensure the Froude scaling of the first natural vibration frequency of a Mark III structural panel, has been clamped in a stiff stainless steel wall. Strain gauges along the deformable plate centerline measure the structural load. To properly characterize the hydroelastic effects, the same experiments have been performed in a fully rigid tank, i.e., by substituting the deformable plate with a stiff plate, and by using pressure transducers to measure the dynamic load along the wall. A ramp function on the sinusoidal motion of the tank forces the flip-through event to occur at the third cycle of oscillation, after a first impact on the opposite wall. The study emphasizes that the hydroelastic evolution is characterized by three different regimes which vary from the quasi-static deformation of the beam in regime I to a strong and fully coupled hydroelastic interaction in regime II and to a free-vibration regime in regime III which ends the dynamic evolution.

The three regimes are detailed with the aid of figures and movies illustrating the kinematics of the flow and the dynamic evolution of the beam deformation (in the elastic case) and of the local pressure (in the rigid case). In particular, during regime I the quasi-static hydrodynamic load induces a small and quasi-static deformation of the beam. A strong and fully coupled hydroelastic behavior follows in regime II; the rapid increase of the hydrodynamic load originates the maximum strain. As a consequence of the structural reaction, the hydrodyanamic pressure still increases. The varying wetted length of the beam causes a variation of the added-mass term and then of the natural vibration frequency of the deformable plate. When the elastic plate is fully wetted the natural frequency remains constant characterizing the free-vibration regime III.

A numerical-experimental model, called *hybrid model*, has been proposed in order to model the structural load. Such model couples the unsteady Euler beam-theory with the forcing term given by the experimental pressure measured in the rigid case. The added mass term is calculated using a potential flow model for incompressible liquid and assuming a quasi-static variation of the free surface. The instantaneous wetted length of the beam is determined by the experimental images. The comparison against experimental data confirms an overall satisfactory prediction of the model. However, differences appear in regime II where a more refined hydroelastic model is necessary.

More simplified theoretical models, typically used at the design stage, have also been implemented and compared with the experimental data. They show an error similar to that of the hybrid model for the prediction of the maximum structural stress when dynamic hydroelastic effects are taken into account. In any case they are not capable to correctly predict the subsequent evolution of the plate deformation.

ACKNOWLEDGMENTS

This research activity has been partially supported by the Research Council of Norway through Centre for Ships and Ocean Structures (CeSOS), and presently ongoing within the Centres of Excellence funding scheme AMOS, Project No. 223254. It has also been in part supported by the Flagship Project RITMARE – The Italian Research for the Sea – coordinated by the Italian National Research Council and funded by the Italian Ministry of Education, University and Research within the National Research Program 2011-2013. A special thanks to Mr. Roberto Zagaglia for his professional skill in the design of the lateral wall with the elastic plate.

The authors are grateful to Professor Maurizio Brocchini of University "Politecnica delle Marche" for his valuable contribution in improving the English language of the text.

[1] B. C. Abrahamsen, "Sloshing induced tank-roof impact with entrapped air pocket," Ph.D thesis (NTNU, 2010).
[2] B. C. Abrahamsen and O. M. Faltinsen, "The effect of air leakage and heat exchange on the decay of entrapped air pocket slamming oscillations," Phys. Fluids **23**(10), 102107 (2011).
[3] A. Colagrossi, G. Colicchio, C. Lugni, and M. Brocchini, "A study of violent sloshing wave impacts using an improved SPH method," J. Hydraul. Res. **48**, 94–104 (2010).
[4] C. Lugni, M. Miozzi, M. Brocchini, and O. M. Faltinsen, "Evolution of the air cavity during a depressurized wave impact. I. The kinematic flow field," Phys. Fluids **22**, 056101 (2010).
[5] C. Lugni, M. Brocchini, and O. M. Faltinsen, "Evolution of the air cavity during a depressurized wave impact. II. The dynamic field," Phys. Fluids **22**, 056102 (2010).
[6] C. Lugni, M. Brocchini, and O. M. Faltinsen, "Wave impact loads: the role of the flip-through," Phys. Fluids **18**(1), 122101 (2006).
[7] O. M. Faltinsen and A. N. Timokha, *Sloshing* (Cambridge University Press, 2010).
[8] E. Marino, C. Lugni, and C. Borri, "A novel numerical strategy for the simulation of irregular nonlinear waves and their effects on the dynamic response of offshore wind turbines," Comput. Methods Appl. Mech. Eng. **255**, 275–288 (2013).
[9] C. Brebbia and J. Dominguez, *Boundary Elements: An Introductory Course* (WIT Press, Boston, Southampton, 1998).
[10] Lloyd Register, "Sloshing assessment guidance document for membrane tank LNG operations," Additional Design Procedures, Version 2.0, May 2009.
[11] Det Norske Veritas, "Sloshing analysis of LNG membrane tanks," Classification Notes No. 30.9, 2006.
[12] D. H. Peregrine, "Water wave impact on walls," Ann. Rev. Fluid Mech. **35**, 23–43 (2003).
[13] M. J. Cooker and D. H. Peregrine, "Pressure-impulse theory for liquid impact problems," J. Fluid Mech. **297**, 193 (1995).
[14] M. Antuono, B. Bouscasse, A. Colagrossi, and C. Lugni, "Two-dimensional modal method for shallow-water sloshing in rectangular basins," J. Fluid Mech. **700**, 419–440 (2012).
[15] B. Bouscasse, M. Antuono, A. Colagrossi, and C. Lugni, "Numerical and experimental investigation of nonlinear shallow water sloshing," Int. J. Nonlinear Sci. Numer. Simul. **14**(2), 123–138 (2013).
[16] N. E. Huang, Z. Shen, S. R. Long, M. C. Wu, H. H. Shih, Q. Zeng, N. C. Yen, C. C. Tung, and H. H. Liu, "The empirical mode decomposition and the Hilbert spectrum for nonlinear and non-stationary time series analysis," Proc. R. Soc. London, Ser. A **454**, 903–995 (1998).
[17] B. Pillon, M. Marhem, G. Leclere, and G. Canler, "Numerical approach For structural assessment of LNG containment systems," in *Proceedings of the Nineteenth International Offshore and Polar Engineering Conference on First ISOPE Sloshing Dynamics and Design Symposium, Osaka, Japan* (ISOPE, Cupertino, CA, 2009), Vol. 3, pp. 175–182.
[18] E. Gervaise, P. E. De Seze, and S. Maillard, "Reliability-based methodology for sloshing assessment of membrane LNG vessels," *Proceedings of the Nineteenth International Offshore and Polar Engineering Conference on First ISOPE Sloshing Dynamics and Design Symposium, Osaka, Japan* (ISOPE, Cupertino, CA, 2009), Vol. 3, pp. 183–191.
[19] *Using Straus7 Manual* (G+D Computing Pty Ltd., Sydney, Australia, 1999).